EES Catalysis

PAPER

View Article Online
View Journal

Cite this: DOI: 10.1039/d6ey00044d

Unraveling electrochemical glycine conversion pathways for ammonia recovery from organic waste

Haldrian Iriawan, †*[a] Jedidian Adjei, †[bc] Danae A. Chipoco Haro, †[d] Dayana Donneys Victoria,[c] Asa G. Ashley,[e] Andrew J. Medford, *[f] Marta C. Hatzell, *[g] Gerardine G. Botte *[bc] and Yang Shao-Horn *[aehi]

Electrochemical conversion of nitrogen-containing organics in sludge offers a route for ammonia recovery but is challenged by compositional complexity. Glycine, abundant in municipal wastewater and structurally simple, provides a model system to benchmark nitrogen and carbon product distributions and electrode stability. Here, we report a coordinated cross-institutional study to elucidate glycine electro-oxidation pathways to ammonia. In alkaline electrolyte, ammonia was produced preferentially under oxidative potentials (>1.60 V_{RHE}), rather than reductive conditions (<−0.40 V_{RHE}), with Ni exhibiting lower overpotentials than Au and Pt. At 2.00 V_{RHE}, ammonia was the dominant nitrogen product (~70%), but with moderate Faradaic efficiency (23.5 ± 2.5%), accompanied by NO_2^-/NO_3^- (~24%), Ni dissolution (~12%), and O_2 evolution (~40%), collectively closing the charge balance. Carbon analysis using HPLC, IC, and ^{13}C NMR revealed a mix of glycolate, glyoxylate, formaldehyde, cyanide, and formate (~20% carbon, 6% Faradaic efficiency), with the remainder as CO_2, indicating concurrent C–N and C–C cleavage pathways. These data, combined with thermodynamic analysis, inform a unified reaction framework and reveal C–N cleavage as the rate-limiting step. Furthermore, the ammonia-dominated production and coupled Ni^{2+} dissolution are correlated across different amino acids, highlighting Ni-complexation as a possible underlying mechanism favoring ammonia production. This work establishes a product-resolved framework and assesses experimental parameters (stirring, cell geometry, potential pulsing) to improve reproducibility and advance mechanistic understanding of ammonia recovery from organic nitrogen electrolysis.

Received 6th March 2026,
Accepted 5th May 2026

DOI: 10.1039/d6ey00044d

rsc.li/eescatalysis

Broader context

Electrified nutrient recovery from municipal waste streams is emerging as a promising strategy to transform wastewater treatment infrastructure into distributed platforms for circular fertilizer production. However, the complex and variable composition of these waste streams presents major challenges for catalyst evaluation, mechanistic understanding, and reliable product quantification. Amino acids are the key building blocks of proteins and dominant nitrogen-containing components of waste sludge. Yet even for the simplest amino acids, such as glycine, fundamental knowledge of nitrogen and carbon product distributions, selectivity, and catalyst stability remains limited. In this work, we establish a reproducible experimental framework across laboratories to examine the electrolysis of glycine and other amino acids, and uncover unexpected ammonia formation as the dominant N product under strongly oxidative conditions, despite the strong thermodynamic driving force to form oxidized products. Comprehensive characterization of reaction byproducts and systematic experimental evaluation provide key mechanistic insights into C–N bond cleavage and hydrogenation steps governing ammonia formation, while highlighting the critical influence of reaction environment and operating parameters on catalyst stability and selectivity. These findings lay the foundation for scalable electrochemical strategies to recover ammonia from organic waste streams, advancing circular nitrogen management and electrified waste treatment.

[a] Department of Materials Science & Engineering, Massachusetts Institute of Technology, Cambridge, MA, 02139, USA. E-mail: haldrian@mit.edu
[b] Department of Chemical Engineering, Texas Tech University, Lubbock, TX 79409, USA
[c] Institute for Sustainability & Circular Economy, Texas Tech University, Lubbock, TX 79409, USA
[d] School of Materials Science and Engineering, Georgia Institute of Technology, Atlanta, GA, 30332, USA
[e] Research Laboratory of Electronics, Massachusetts Institute of Technology, Cambridge, MA, 02139, USA
[f] School of Chemical & Biomolecular Engineering, Georgia Institute of Technology, Atlanta, GA, 30332, USA
[g] George W. Woodruff School of Mechanical Engineering, Georgia Institute of Technology, 770 Ferst Ave, Atlanta, GA, 30309, USA
[h] Department of Mechanical Engineering, Massachusetts Institute of Technology, Cambridge, MA, 02139, USA
[i] Department of Chemistry, Massachusetts Institute of Technology, Cambridge, MA, 02139, USA
† Equally contributing authors.

Introduction

Recovering ammonia from nitrogen-containing organic wastes is an increasingly attractive strategy to couple waste management with nutrient circularity. Municipal and agricultural waste streams contain substantial amounts of organically bound nitrogen that are removed during conventional biological treatments rather than recovered as fertilizer precursors.[1] As a widely implemented biological process, an activated sludge treatment entails enzymatic mineralization of organic-N to ammonium (NH_4^+) *via* microbial hydrolysis and deamination.[2] The resulting NH_4^+ is oxidized to nitrite/nitrate by microorganisms, followed by reduction to N_2 (denitrification),[2,3] resulting in irreversible nitrogen loss and often requiring external electron donors such as carbon black to sustain complete denitrification.[4] The conventional activated sludge processes are also energy intensive, where aeration represents the dominant electricity demand (often reported as ~45–75% of energy cost).[5]

Electrochemical approaches offer an attractive route in which chemical transformations are driven directly by applied potential and powered by electricity, enabling flexible operational control and coupling to renewables.[6,7] Compared to thermal routes for sludge conversion (*e.g.*, pyrolysis/gasification), which typically operate at ~300–1000 °C and demand centralized heat integration and solid-handling infrastructure,[8,9] or plasma-assisted routes which rely on specialized reactors and high-energy excitation,[10] electrolysis can operate near ambient conditions and allows modular, decentralized deployment at wastewater treatment facilities.[11] Jafari and Botte demonstrate that the electrochemical treatment of waste-activated sludge can produce ammonia (NH_3) alongside short-chain fatty acids using electrodes including Ni, Cu, and stainless steel at low potentials (~1.35 V *versus* Hg/HgO) in alkaline media (0.2 M NaOH), or ~2.2 V *versus* reversible hydrogen electrode, V_{RHE}, assuming pH = 13.[12] Notably, Ni electrodes are reported to yield 250 mg L^{-1} of ammonia after 2 h of pulsed electrolysis.[12] Technoeconomic analyses of electrically-assisted sludge conversion using these experimental findings reveal electrolysis as a promising route for sludge valorization and nutrient recovery, with potential advantages in integration simplicity, distributed operation, and compatibility with intermittent electricity.[6]

A central challenge in valorizing wastewater-derived feedstocks is that sludge composition varies widely with source, thus complicating product distribution and electrode stability analyses. In sewage sludge, the total solids (TS) content is typically 2–9%, of which organic solids account for approximately 20–44%.[13] Within this organic fraction, carbon constitutes roughly 20–40% of TS,[13–16] while total nitrogen is present at 2.8–4.9%.[13,14,16,17] Proteins represent a dominant component of the organic matter (40–60%),[18] alongside polysaccharides, lipids, and fatty acids.[19] At alkaline conditions, proteins can be depolymerized into their constituent amino acids, and analyses of waste-activated sludge have identified ~18 amino acids with distinct compositional distributions (see Table 1).[20] As the highest nitrogen-density fraction of sludge, proteins and their amino acid building blocks are therefore attractive targets for electrochemical upgrading strategies aimed at ammonia recovery. Of these, glycine is a practical model molecule for two reasons: it is one of the most abundant amino acids in municipal sludge and extracellular polymeric substances, and it is the simplest amino acid, containing only an amine and a carboxylate group with no side chains. This minimal chemical complexity makes glycine an ideal benchmark system for isolating how experimental variables influence key observables such as nitrogen and carbon product distributions, Faradaic efficiencies, and electrode stability.

Table 1 Amino acid composition of waste activated sludge, expressed as a percentage of the crude protein portion of the sludge[20]

Amino acid	wt% of crude protein in sludge
Aspartic acid (Asp)	8.3
Glutamic acid (Glu)	8.1
Alanine (Ala)	7.3
Leucine (Leu)	5.6
Glycine (Gly)	4.9
Threonine (Thr)	4.2
Valine (Val)	4.1
Serine (Ser)	3.4
Lysine (Lys)	3.3
Proline (Pro)	3.1
Phenylalanine (Phe)	3.1
Arginine (Arg)	2.9
Isoleucine (Ile)	2.7
Tyrosine (Tyr)	2.4
Cystine (Cys)	2.1
Methionine (Met)	1.45
Tryptophan (Trp)	0.8
Histidine (His)	0.6

Electrochemical glycine oxidation has been explored on a range of electrode materials, including Pt, Au and more recently Ni-based metals. The oxidation of glycine on Pt has been extensively investigated. For example, Marangoni *et al.* have studied glycine (at 0.45 M) on Pt at both pH 1 and 13 *via* cyclic voltammetry and constant potential measurements, whose findings lead to mechanisms involving glycine adsorption through the carboxyl group followed by CO_2 evolution and methylamine to form ammonia and formaldehyde.[21] The ammonia selectivity at pH 13 at 1.06 V_{SCE} (*i.e.* ~1.8 V_{RHE})[21] was reported at ~83%, although the number of electrons (n_{e^-}) in the calculation was not specified and the ammonia detection *via* the Kjeldahl method[22] could be interfered with by organic N as well as $NO_{2/3}^-$.[23] The proposed mechanism of glycine oxidation on Pt[24] and Au[25] is supported by *in situ* vibrational spectroscopy, revealing the glycine adsorption by the COO^- down configuration and reaction intermediates such as CN^- and CNO^-, alongside the detected reaction products such as CO_2 and NH_3. However, the quantification of ammonia efficiency and product distribution is not reported. More recently, Ni-based electrodes that can convert surface $Ni(OH)_2$ (Ni(II)) to NiOOH (Ni(III)) upon oxidation and effectively oxidize urea[26,27] and alcohols,[28] are reported for glycine oxidation, including doped $Ni(OH)_2$ catalysts such as $Ni_{0.77}Co_{0.20}Cd_{0.03}(OH)$[29] and $Ni_{1.5}Mn_{1.5}O$.[29] Furthermore, amino acid conversion to ammonia, including glycine, was reported to have enhanced charge efficiency by potential pulsing on Au and Ni,[30] an established

strategy in enhancing the turnover of the desired products as demonstrated in CO_2 reduction to C^{2+} products,[31] NO_3^- reduction to NH_4^+,[32] and urea oxidation.[27] Despite these reports, systematic analyses of reaction products generated during glycine oxidation on metals, of electrode stability in the presence of glycine and N-containing ligands, and of the impact of experimental conditions on the measured Faradaic efficiencies, are lacking.

In this work, we have performed a coordinated cross-institutional study to investigate experimental details of electrochemical glycine conversion to ammonia. Three independent labs at different institutions have executed a nominally identical protocol spanning cell/component cleaning, electrode treatment, reference electrode calibration, electrochemical operation, and product quantification. With the shared benchmarking effort, using polished Ni foil in 0.1 M KOH + 0.1 M glycine, ammonia was detected under oxidative potentials (>1.60 V_{RHE}). At 2.00 V_{RHE}, ammonia dominates the solution-phase nitrogen products ($\sim$70% of the N-product distribution) with ammonia Faradaic efficiency (FE) of 23.5 $\pm$ 2.2% across institutions, but this selectivity is accompanied by parasitic reactions including substantial Ni dissolution ($>$12%), formation of oxidized nitrogen products ($NO_{2/3}^-$, $\sim$24%), and O_2 evolution ($\sim$40%), cumulatively leading to complete charge balance. Comprehensive carbon analysis *via* high performance liquid chromatography (HPLC), ion chromatography (IC), and carbon nuclear magnetic resonance (^{13}C-NMR) revealed multiple oxidation products such as glycolate, glyoxylate, formaldehyde, cyanide, formate, and CO_2 in the form of carbonate (CO_3^{2-}) indicating parallel pathways involving C═N and C–C scission in glycine activation. Furthermore, extending the study to alanine, lysine, and aspartic acid revealed that ammonia-dominated production was correlated with Ni^{2+} dissolution, highlighting Ni complexation as a possible origin of ammonia-dominated production. Critically, nitrogen selectivity, Ni corrosion rates, and carbon product distribution were found to depend on experimental conditions such as stirring rate, electrode area, cell architecture, and potential pulsing, demonstrating the strong influence of local reaction environment and underscoring the need for exhaustive reporting and community-facing best-practice protocols. Recommended experimental practices are discussed to improve reproducibility and accelerate the mechanistic understanding of electrochemical amino acid conversion towards scalable ammonia recovery from organic waste.

Experimental section

Electrochemical glycine oxidation measurements

Nickel foil electrodes (0.25 mm thick, annealed, 99.5% metal basis, Thermo Scientific) cut into 1 $\times$ 0.5 cm^2 pieces were electropolished prior to electrochemical measurements *via* a two-electrode setup in 85% *ortho*-phosphoric acid (Sigma-Aldrich), with Ni foil as the working electrode and a Pt or Ti mesh as the counter electrode at 3.0 V for 5 min. The current recorded was around 30 mA. The foil was then thoroughly rinsed with ethanol, wiped clean, and dried at 60 °C. For testing with Pt (0.1 mm thick, 99.99% metal basis, Sigma) and Au (0.1 mm thick, 99.95% metal basis, Thermo Scientific), the electrodes were sonicated in deionized water and dried overnight prior to use.

Electrochemical glycine oxidation experiments were conducted in a two-compartment H-cell, separated by an anion exchange membrane (DSVN, thickness = 95 μm, Bellex International Corp.) with both compartments containing 0.1 M as-received KOH (semiconductor grade, 99.99% trace metals basis, Sigma Aldrich) and 0.1 M glycine ($\geq$99%, Sigma Aldrich). Hg/HgO or Ag/AgCl reference electrodes were employed, and a Pt mesh (99.99%, StonyLab) served as the counter electrode. Prior to glycine experiments, the Ni working electrode was electrochemically conditioned by cycling through the oxygen evolution region (1.10–1.70 V_{RHE}) for 25 cycles in glycine-free electrolyte (0.1 M KOH). Then, electrolytes were replaced and the working electrode compartment was bubbled with Ar (99.999%, Airgas or Linde) for 20 min at 20 sccm before the start of electrolysis; the step-by-step protocol can be found in Note S1. The potentials reported against RHE follow eqn (1), where the electrolyte pH was consistently measured to be 10.7 *via* a pH meter. To maintain a consistent applied potential during the potential holds and to prevent overcompensation at high currents caused by auto compensation (an issue previously reported),[33] the voltage was manually corrected for the IR drop. The solution resistance used for this correction was determined from the high-frequency real-axis intercept obtained by impedance spectroscopy measurements conducted after 15 minutes, 30 minutes, 1 hour, and 2 hours of electrolysis. The applied electrochemical potentials were converted to the reversible hydrogen electrode scale (V_{RHE}) using the following equation:

$$V_{RHE} = V_{meas} + V_{ref} + 0.059 \times pH - IR \quad (1)$$

where V_{meas} is the potential difference measured between the working electrode and the reference electrode used during electrolysis, V_{ref} is the potential difference between the standard hydrogen electrode and the reference electrode used in the experiments (*i.e.* +0.210 V for Ag/AgCl 3 M KCl, +0.197 V for Ag/AgCl (sat. KCl) or +0.098 V for Hg/HgO with 4.24 M KOH at 25 °C),[34] and IR is the potential drop from solution resistance. We note that the RHE conversion *via* pH has been chosen over the HER/HOR method on Pt due to the apparent surface poisoning of Pt by glycine, which shifted the zero-current intercept (see discussion in Note S2 and Fig. S1). During electrolysis, the working compartment was stirred with a PTFE 10 mm stir bar with a 3 mm diameter at 300 rpm. 3.0 mL of electrolytes were sampled at the 15 min, 30 min, 1 hour, and 2 hours intervals with replacement. Between experiments, the H-cell was thoroughly rinsed with deionized water (18.2 MΩ cm, Millipore) and dried, while the membrane was stored in deionized water. Periodic deep cleaning was performed approximately monthly by overnight (12 hours) soaking in aqua regia, followed by boiling at $>$200 °C for $>$ 30 min in deionized water.

Other amino acids tested were 0.1 M lysine (L, Sigma, ≥98%), 0.1 M alanine (L, Sigma, ≥99.5% BioUltra), and 0.05 M aspartic acid (L, 99%, BioXtra), where the experimental procedure was identical to that of glycine.

Product quantification

Ammonia (NH_3) in the glycine electrolyte was quantified as ammonium (NH_4^+) using nuclear magnetic resonance (NMR) and ion chromatography (IC). We note that the presence of glycine significantly suppressed the blue color formation of the indophenol blue in the presence of ammonia (Fig. S2), rendering it ineffective for reliable quantification. Both ^{1}H-NMR and IC quantification were found to be reliable (see calibration curves in Fig. S3–S7). Therefore, ammonia quantification was managed independently at each laboratory, while cross-validation was performed at the Faradaic efficiency level considering the likely larger contributions of error from other experimental factors such as variations in the *iR*-corrected potential during electrolysis and electrode and analyte preparations (*e.g.* dilution errors).

Nuclear-magnetic resonance. At institution 1, NH_4^+ was quantified *via* ^{1}H-NMR using 500.18 MHz Bruker AVANCE NEO spectrometer. 500 μL of the analyte was mixed with 50 μL of 4.0 M HCl, 25 μL of 3 mM maleic acid and 63.9 μL D_2O. Acquisition of ^{1}H-NMR spectra was performed using the solvent suppression program with 128 scans and 2 s delay per scan. NH_4^+ calibration curve used for quantification and representative spectra post-electrolysis can be found in Fig. S3 and S4. Ammonia in the acid trap was generally found to be minimal, 2 orders of magnitude lower than the ammonia in the electrolyte (see Fig. S5). Therefore, the Faradaic efficiencies reported utilized ammonia in the electrolyte.

Ion-chromatography. The specific instrument column configurations at institutions 2 and 3 can be found in the SI, with each configuration yielding reliable NH_4^+ calibrations (Fig. S6 and S7) prepared from ammonium standards (99.999% NH_4Cl, VeriSpec®). At institution 2, electrolysis samples were acidified with 1 M HCl and diluted 100 times with DI water, and the samples were measured with 15 mM methanesulfonic acid eluent at 0.25 mL min^{-1} at 25 °C. At institution 3, samples were detected without acidification and dilution, and measured with 30 mM methanesulfonic acid as the eluent at 30 °C. The acquisition and evaluation of chromatograms were carried out with the software Chromeleon (Thermo Scientific).

All three institutions employed anion chromatography with a conductivity detector to measure nitrate (NO_3^-) and nitrite (NO_2^-), where the specific instrument column configurations can be found in the SI and each independently yielded linear calibration curves against NO_3^- and NO_2^- standards of known concentrations (Fig. S8 and S9). At institution 1, 250 μL samples were diluted by a factor of 2 with deionized water and measured at 0.25 mL min^{-1} of sodium carbonate and bicarbonate eluent. At institution 2, samples were diluted 100 times with deionized water and measured at 0.15 mL min^{-1} of the same eluent. At institution 3, 25 μL of standard solution was injected into the eluent stream. The flow rate was maintained at 1.0 mL min^{-1} under a linear gradient elution from 20 mM to 40 mM KOH.

Ni dissolution was measured *via* inductively-coupled plasma-mass spectrometry (ICP-MS, institution 1) and ICP-OES (institutions 2 and 3), for which linear calibration curves as a function of Ni^{2+} concentration (ICP standard) were achieved (Fig. S10) and independently generated for each ICP measurement. Samples were diluted with a factor of 5–500 in 2% HNO_3 (ICP grade).

Gas quantification was performed by connecting the H-cell to a SpectroInlet electrochemistry mass spectrometer (EC-MS) Professional, which was equipped with a quadrupole mass spectrometer (QMG 250, Pfeiffer). A Spectro Inlet aqueous chip enabled gaseous products to enter the mass spectrometer; all other openings were sealed except the connection to the H-cell (Fig. S11). During operation, Ar was continuously flowed through the system at 30 mL min^{-1}. Prior to measurements, signals were recorded for 10 min to establish a stable baseline, after which the electrochemical program was initiated. For quantification, an O_2 calibration curve was constructed by performing oxygen evolution on Ni foil in 0.1 M KOH. Constant current steps (30, 20, 10, 5, and 2.5 mA) were applied, with open-circuit intervals between each step to allow signal to decay back to the baseline level. The mass spectrometry signal at m/z = 32 was then correlated with the expected O_2 production (assuming 100% Faradaic efficiency with z_{e^-} = 4, see Table 2) to generate calibration curves for both O_2 production rate (μmol s^{-1}) and total O_2 evolved (μmol), exhibiting excellent linearity (see Fig. S12). This calibration was subsequently used to convert OER signals obtained during amino acid oxidation.

Carbon products were independently detected at the three institutions to determine key reaction byproducts during glycine electrolysis. At institution 1, ^{13}C-NMR was employed for which the glycine electrolysis was performed following the same electrochemical protocol but instead used $^{13}C_2$ glycine (99 atom% ^{13}C, Sigma) where the two carbons are labelled. 500 μL sample was mixed with 50 μL D_2O and measured with 500.18 MHz Bruker AVANCE NEO spectrometer. Spectra were acquired using a zgdepq pulse sequence with broadband ^{1}H decoupling. A total of 512 scans were accumulated with a relaxation delay of 1.0 s over a spectral width of 30 kHz (~240 ppm), centered at 100 ppm. At institution 2, high-performance liquid chromatography was used with HPX-87H organic acid analysis column (AMINEX) paired with Biorad, equipped with a UV-vis detector positioned at 260 nm (2489 UV/Vis Detector, Waters). The eluent was 5 mM H_2SO_4, the column flow rate was 0.4 mL min^{-1} and the column temperature was 30 °C. At institution 3, anion chromatography was used to identify and quantify detected carbon products such as glycolate, formate, acetate, glyoxylate, and oxalate using gradient elution, where the temperature (30–50 °C), elution time, and KOH concentrations for linear gradient were optimized for each carbon product which resulted in linear calibration curves (Fig. S13). Full details of instrument configuration can be found in the SI. Cyanide quantification was done with the Pyridine barbituric acid method (see SI). Chemical Oxygen Demand

Table 2 z per product for FE calculations from electrochemical glycine oxidation

Compound	z	Equations
Ni	2	$Ni_{(s)} \rightarrow Ni^{2+} + 2e^-$
NH_3	6	$NH_2CH_2COOH + 2H_2O \rightarrow NH_3 + 2CO_2 + 6H^+ + 6e^-$ (acid) $NH_2CH_2COO^- + 5OH^- \rightarrow NH_3 + 2CO_2 + 3H_2O + 6e^-$ (alkaline)
NO_2^-	12	$NH_2CH_2COOH + 4H_2O \rightarrow NO_2^- + 2CO_2 + 13H^+ + 12e^-$ $NH_2CH_2COO^- + 12OH^- \rightarrow NO_2^- + 2CO_2 + 8H_2O + 12e^-$
NO_3^-	14	$NH_2CH_2COOH + 5H_2O \rightarrow NO_3^- + 2CO_2 + 15H^+ + 14e^-$ $NH_2CH_2COO^- + 14OH^- \rightarrow NO_3^- + 2CO_2 + 9H_2O + 14e^-$
O_2	4	$2H_2O \rightarrow O_2 + 4H^+ + 4e^-$ $4OH^- \rightarrow O_2 + 2H_2O + 4e^-$
CN^-	4	$NH_2CH_2COOH \rightarrow CN^- + CO_2 + 5H^+ + 4e^-$ $NH_2CH_2COO^- + 4OH^- \rightarrow CN^- + CO_2 + 4H_2O + 4e^-$
Glyoxylic acid	2	$NH_2CH_2COOH + H_2O \rightarrow OCH–COOH + NH_3 + 2H^+ + 2e^-$ $NH_2CH_2COO^- + 2OH^- \rightarrow OCH–COO^- + NH_3 + H_2O + 2e^-$
Glycolic acid	2[a]	$OCHCOOH$ (glyoxylic acid) $+ 2H^+ + 2e^- \rightarrow HOCH_2COOH$ (glycolic acid) (net) $NH_2CH_2COOH + H_2O \rightarrow HOCH_2COOH + NH_3$ (net) $NH_2CH_2COO^- + H_2O \rightarrow HOCH_2COO^- + NH_3$
Formic acid	4	$NH_2CH_2COOH + 2H_2O \rightarrow HCOOH + CO_2 + NH_3 + 4H^+ + 4e^-$ $NH_2CH_2COO^- + 4OH^- \rightarrow HCOO^- + CO_2 + NH_3 + 2H_2O + 4e^-$

[a] Since glycolic acid/glycolate is a 2-electron reduction from glyoxylic acid/glyoxylate, $n_{e^-} = 2$ for the glycine-to-glyoxylate conversion has been used in the faradaic efficiency calculation of glycolate.

(COD) was attempted but suffered from significant interference from glycine, glyoxylic acid and formic acid (see SI and Fig. S14).

Faradaic efficiency calculations

The Faradaic efficiency (FE) of N-products (NH_3, NO_2^-, and NO_3^-), metal products (Ni), and C-products were calculated by the following equation:

$$FE_i = \frac{z_i \times n_i \times F}{Q} \quad (2)$$

where z_i is the number of electrons used for the transformation, assuming complete oxidation of the carbon to CO_2 for the nitrogen conversions to act as an upper-bound, as specified in Table 2; n_i is the number of moles of product i, F is the Faraday constant (96 484 C mol^{-1}), and Q is the amount of charge transferred during the reaction.

Results and discussion

Benchmarking of electrochemical glycine oxidation

A shared electrochemical protocol, executed independently across three different laboratories, hereafter referred to as institution 1–3 (Fig. 1a), revealed ammonia as the dominant product of glycine electrolysis on nickel (Ni) at oxidative potentials. To enable meaningful benchmarking across laboratories, several experimental checkpoints were enforced prior to glycine electrolysis, which included consistent and overlapping cyclic voltammograms of Ni foil in the glycine-containing electrolyte (Fig. S15) as well as aligned RHE potential conversion after iR correction (see demonstration in Fig. S16). The latter required the consideration of solution resistance, which depended on the H-cell assembly, the accurate pH measurement of the glycine-containing electrolytes and rigorous reference electrode calibration (see Note S2 and Fig. S1). Under these conditions, electrolysis at 2.00 V_{RHE} after iR-correction (with variations of on average ± 30 mV over the 2 hours, see Fig. S17–S19 and Table S1) in 0.1 M KOH and 0.1 M glycine consistently produced ammonia as the predominant nitrogen-containing product across all three institutions. Specifically, NH_3 accounts for approximately 60–70% of the solution-phase nitrogen product distribution, while the remaining ~30% consists of NO_3^- and NO_2^- (Fig. 1b). These observations are robust across independent repeats at each institution, demonstrating agreement in the production levels of NH_3, NO_2^- and NO_3^- (Fig. S20–S22). In addition, by connecting the H-cell to a mass spectrometer (Fig. S18), only O_2 (m/z = 32) was detected while other gas-phase products such as N_2 or CO (m/z = 28), NO (m/z = 30), and CO_2 (m/z = 44) were not observed above experimental uncertainty (Fig. S18). CO_2 was found to instead reside in the electrolyte as CO_3^{2-}, which was characterized further (see 'Carbon product characterization' section). We note that one aspect not initially controlled in the benchmarking was the stir bar size, which was found to considerably influence product selectivity (see later section). The formation of oxidized nitrogen species is not unexpected given the highly oxidative potential applied, which exceeded the thermodynamic redox potential of NH_3/NO_3^- (E^0 = 0.88 V_{RHE})[35] and N_2/NO_3^- (E^0 = 1.24 V_{RHE}),[36] and under which the oxidation of urea[37,38] or ammonia[27] to NO_3^-, NO_2^-, or N_2 has previously been associated with the $Ni(OH)_2$ to NiOOH transformation. Nevertheless, the dominance of ammonia suggests that it is comparatively stable under these conditions, preferentially remaining in the electrolyte rather than undergoing further oxidative conversion to NO_2^- and NO_3^-.

Ammonia formation was found to increase linearly over the 2 h electrolysis at 2.00 V_{RHE} as a function of charge passed (Fig. 1c). The assignment of ammonia as a glycine-derived product was further corroborated by isotope-labelling experiments using commercially available ^{15}N-glycine, which showed a quantitative agreement in the ammonia production relative to experiments with unlabeled glycine (Fig. S23 and S24). However, alongside abundant $^{15}NH_3$, a non-negligible fraction of $^{14}NH_3$ was also detected, which suggests isotopic or nitrogen

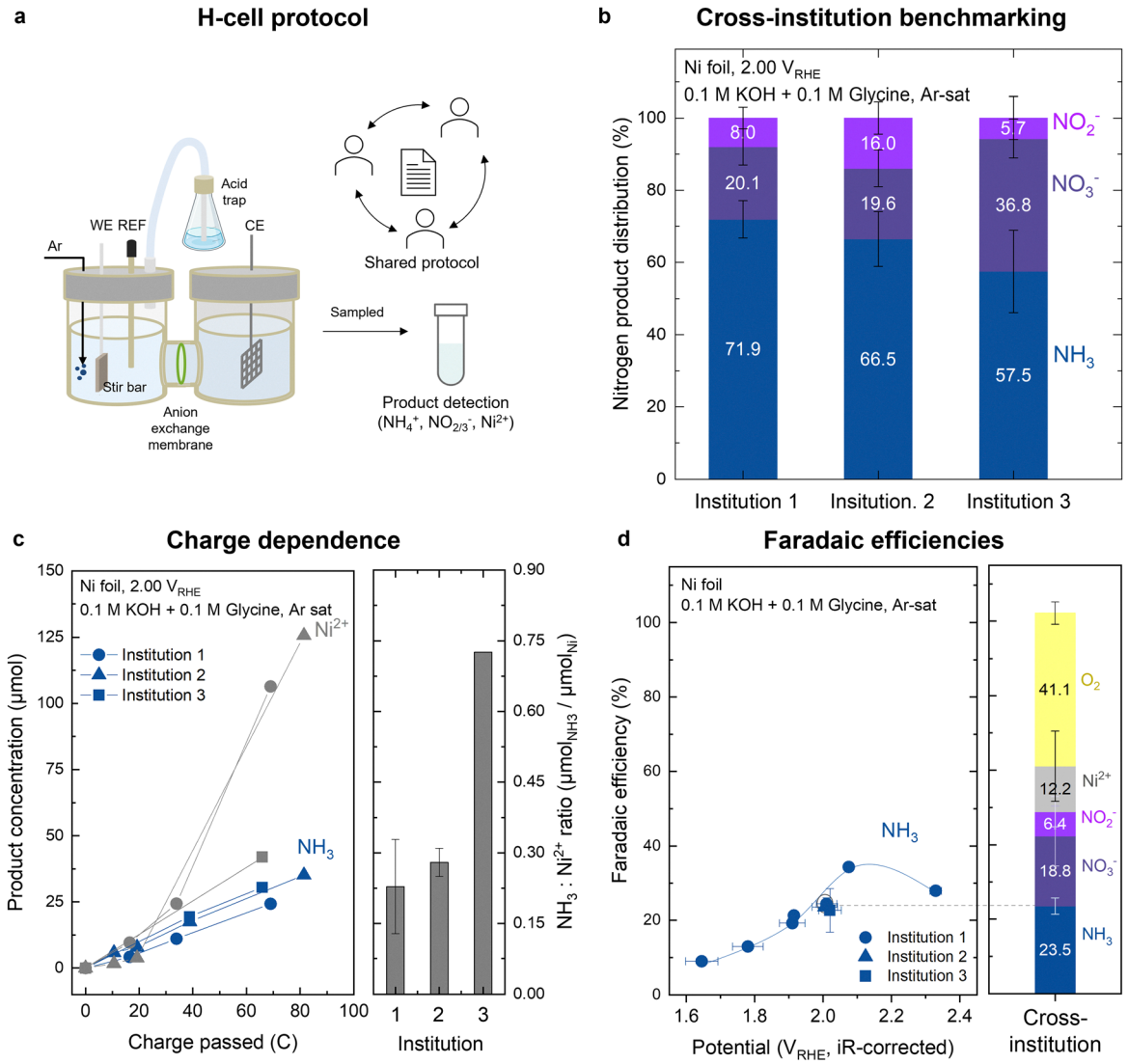

Fig. 1 Experimental benchmarking of electrochemical glycine oxidation on Ni. (a) H-cell setup for electrochemical glycine oxidation with Ni foil at 2.00 V_{RHE} 0.1 M KOH + 0.1M glycine (Ar-sat). (b) cross-institution benchmarking of nitrogen products in the electrolyte, showing ammonia-dominated nitrogen product. Error bars indicate $n \geq 3$ repeats (Fig. S21 and Table S1). It is noted that the benchmarking condition for institution 3 corresponds to no stirring condition, which is more similar to data from institution 1 and 2 using a small stir bar (10 mm at 300 rpm). More discussion can be found in relation to Fig. 4. (c) Time-dependent profile of ammonia (blue, measured *via* Ion chromatography or H-NMR) and Ni corrosion (gray, measured *via* ICP-MS) with respected to cumulative charge passed on Ni foil at 2.00 V_{RHE}, showing significant electrode dissolution alongside ammonia generation. (d) Potential-dependent faradaic efficiency to ammonia, calculated assuming $z_{e^-} = 6$ from $NH_2CH_2COOH + 2H_2O_{(l)} \rightarrow NH_{3(g)} + 2CO_{2(g)} + 6(H^+ + e^-)$, see Table 2. The faradaic efficiency at 2.00 V_{RHE} corresponds to the benchmarking condition over 2 h electrolysis, while the Faradaic efficiencies at other potentials were obtained from the potential screening experiment where 15 min chronoamperometry holds (CA) were conducted over time in the same electrolyte (see Fig. S5). The right panel shows cross-institution cumulative Faradaic efficiencies for the different products, assuming z_{e^-} = 14, 12, 2 and 4 for NH_2CH_2COOH/NO_3^-,CO_2; NH_2CH_2COOH/NO_2,CO_2, Ni/Ni^{2+} and OH^-/O_2 respectively. Details of Faradaic efficiency calculation can be found in Table 2. Tabulated Faradaic efficiency values from the three institutions can be found in Table S1.

impurities in the commercial ^{15}N-labeled glycine, highlighting the need for caution when employing ^{15}N-labeled glycine in mechanistic studies of nitrogen-containing products.

The increase in ammonia was linearly accompanied by significant Ni^{2+} dissolution. The Ni^{2+} concentration in the electrolyte, quantified by ICP after 2 h of electrolysis, reached up to ~120 μmol, which is substantially larger than the ~25–30 μmol of ammonia produced, indicative of ~2–5× more Ni dissolved than ammonia formed. While all three institutions encountered challenges in reliably quantifying dissolved Ni (Fig. S25 and S26), the Ni^{2+} values shown in Fig. 1c were quantified with confidence (see Note S3) and represented the upper bound across trials. Notably, the Ni dissolution without glycine was found to be negligible (<0.1 umol in 0.1 M KOH electrolyte at 2.00 V_{RHE} over 2 hours, see Fig. S27). The glycine-promoted Ni dissolution can be attributed to the exothermic complexation of Ni(II) with glycinate (the deprotonated form of glycine), for which the aqueous complexation enthalpy at 25 °C has been reported as −36.7 kJ mol^{-1}.[39]

Notably, the coupled ammonia production and Ni dissolution could point to a dissolution-mediated pathway for ammonia formation, wherein Ni-ammonia complexation lowers the thermodynamic and/or kinetic barrier of making ammonia. For example, the formation of Ni–NH_3 complex (*i.e.* $Ni^{2+} + 6NH_3 \rightarrow [Ni(NH_3)_6]^{2+}$) has an overall reaction enthalpy of -94.6 kJ mol^{-1} at 25 °C according to DFT computation,[40] indicating strong stabilization of coordinated ammonia, which can stabilize NH_3 in solution from further oxidation to NO_2^- or NO_3^- under the oxidative conditions used in this work. This is discussed further in the screening of other amino acids below. Further mechanistic studies are required to understand how glycine enhances Ni corrosion and whether soluble Ni species facilitate ammonia production under oxidative conditions. Interestingly, prior electrochemical studies on real waste activated sludge under pulsed electrolysis conditions (1.35 V *vs.* Hg/HgO, 0.2 M NaOH, 2 h) did not report significant Ni dissolution,[12] suggesting that the complex matrix of real sludge comprising proteins, polysaccharides, lipids, and extracellular polymeric substances may provide passivation or competitive complexation that protects the Ni surface. The particularly strong complexation of Ni(II) with glycinate may be uniquely aggressive compared to the diverse ligand environment present in real sludge, with important implications for catalyst design: electrode alloys or surface modifications that reduce glycinate complexation may improve stability during amino acid electrolysis. Overall, the high anodic overpotential and Ni instability raise concerns regarding the practical viability of ammonia recovery from amino acids on Ni. Further assessment of electrode stability under continuous operation in more practical setups (*e.g.*, flow cells), as well as understanding and mitigating surface passivation in real sludge, will be important directions for future work.

The ammonia Faradaic efficiency became larger when the working electrode potential was increased from 1.60 to 2.05 V_{RHE}, and then decreased at higher potentials (Fig. 1d). The Faradaic efficiency of ammonia, calculated using eqn (2) with $z_{e^-} = 6$ assuming full oxidation of carbon to CO_2 as an upper bound of efficiency (Table 2), increased from ~10% to ~38%, where the latter was operated at a higher potential than the 2.00 V_{RHE} benchmarking condition, which corresponds to 2.05 V_{RHE} after iR-correction. The logarithm of the ammonia formation rate was found to be proportional to the applied potential between 1.60 V_{RHE} and 2.05 V_{RHE}, with a Tafel slope of 277 ± 22 mV dec^{-1} (Fig. S5). This behavior suggests that ammonia formation is governed either by an electrochemical rate-determining step or by a chemical rate-determining step involving electrochemically-generated active sites. It is noted that the potential (≥1.60 V_{RHE}) needed to produce ammonia (Fig. 1d and Fig. S5) is significantly more positive than the standard thermodynamic potential of glycine oxidation to make ammonia, $NH_2CH_2COOH_{(s)} + 2H_2O_{(l)} \rightarrow 2CO_2 + NH_3 + 6H^+ + 6e^-$, $E^0 = +0.06$ V_{RHE} (see Table S2 for details), indicative of slow kinetics for ammonia production. Nevertheless, Ni foil exhibited a considerably lower oxidative overpotential than Au and Pt, where ammonia production became apparent only at potentials >2.1 V_{RHE} and >2.6 V_{RHE}, respectively (Fig. S5), signifying the surface-dependence of glycine conversion to ammonia. For Ni, the decrease in ammonia FE upon further increase in the potential beyond 2.05 V_{RHE} is not understood. We hypothesize that this may occur due to competing processes such as O_2 evolution and Ni corrosion, and/or lower activity toward glycine oxidation on further oxidized Ni surfaces[41] (*e.g.* NiO_2). On the other hand, reduction at constant potentials such as -0.4 V_{RHE} and below did not show any ammonia production (Fig. S28), suggesting the role of electrochemical oxidation (rather than reduction) in glycine activation, nitrogen liberation and ammonia formation. At the benchmarking condition (representative data shown in the right panel of Fig. 1d), the three institutions consistently reported an ammonia FE of 23.5 ± 2.2%, where the uncertainty was attributed to experimental factors such as variations in the *iR*-corrected potential across trials and electrode and electrolyte preparations (*e.g.* dilution errors). The Faradaic efficiency toward NO_2^-/NO_3^- collectively accounted for comparable percentages of ~25%. A significant portion of charge (on average ~10%) was associated with Ni corrosion while the remaining charge (~40%) was attributed to O_2 evolution, thereby closing the charge balance. Overall, these benchmarking efforts, which are focused on uncovering the Faradaic efficiency and distribution of N products and Ni dissolution, demonstrated consistent cross-institution alignment in capturing the experimental findings of glycine oxidation on Ni. Next, a more detailed understanding of glycine transformation was investigated through multi-technique carbon detection to enable the elucidation of possible reaction pathways during glycine oxidation.

Carbon product characterization

Multiple characterization techniques of the post-electrolysis solutions revealed a diversity of carbon products resulting from electrochemical glycine oxidation. Following the reproducible nitrogen product characterization across the three institutions (Fig. 1), the post-electrolysis electrolytes at 2.00 V_{RHE} were independently analyzed for carbon-containing species. Based on HPLC analysis performed by institution 2, two dominant peaks at retention times of 18.5 min and 20.8 min systematically increased with electrolysis time, which were attributed to glycolic acid and formic acid, respectively, based on comparison with reference spectra (Fig. 2a). Minor peaks at 14.2 min indicated the presence of glyoxylic acid while other minor peaks at 16.4 min, 19.6 min, and 21.8 min could not be assigned, indicative of other carbon products. In addition, anion chromatography using KOH gradient elution developed by institution 2 specifically for this detection confirmed the formation of formate (Fig. 2b), consistent with the HPLC observations. Notably, anion chromatography showed the glyoxylate peak at a retention time of 4.4 min greater than that of glycolate at 12.1 min, opposite to that observed by HPLC, which might be due to subtle differences in mass transport not captured in the benchmarking protocol across institutions (see discussion of Fig. 4 below). Moreover, institution 1 employed ^{13}C NMR spectroscopy after performing the electrolysis with $^{13}C_2$-glycine (both carbon atoms isotope-labeled),

which showed a prominent peak at ~165 ppm, attributable to carbonate ($^{13}CO_3^{2-}$)[42] that came from the dissolution of CO_2 in the basic solution (pH = 10.7 measured for the 0.1 M KOH + 0.1 M glycine electrolyte). To assess the carbon balance, CO_3^{2-} quantification *via* electrolyte acidification showed that it represented 80% of the consumed glycine (Fig. S30–S32), thus validating the assumption that the carbon undergoes full oxidation to CO_2 under the harsh oxidative condition in this work. An NMR peak at ~123 ppm (Fig. 2c) revealed the presence of cyanide (CN^-),[43] which is independently verified by institution 3 *via* colorimetric methods (see Experimental section). Furthermore, several minor NMR peaks were observed: formaldehyde at ~82 ppm[44] and glyoxylate at ~90 ppm,[45] in agreement with HPLC and anion chromatography results (Fig. 2a and b). Formate, although identified as a dominant product by HPLC and ion chromatography, could not be unambiguously resolved by ^{13}C NMR due to overlap with the carboxylate carbon of glycine. The ammonia Faradaic efficiency from electrolysis with $^{13}C_2$ quantitatively matched that with unlabeled glycine, confirming that reproducible conditions were achieved during the product analysis (Fig. S29). Overall, the combined carbon product analyses revealed a diverse set of glycine oxidation products at 2.00 V_{RHE} on Ni, including predominantly formate, glyoxylate, glycolate, formaldehyde, cyanide, and CO_2 in the form of CO_3^{2-}. Identification of these carbon products provides important constraints on the reaction pathways by which glycine is transformed to ammonia.

Reaction pathways of electrochemical glycine oxidation

The diverse experimentally detected carbon byproducts suggest that multiple reaction pathways are operative during

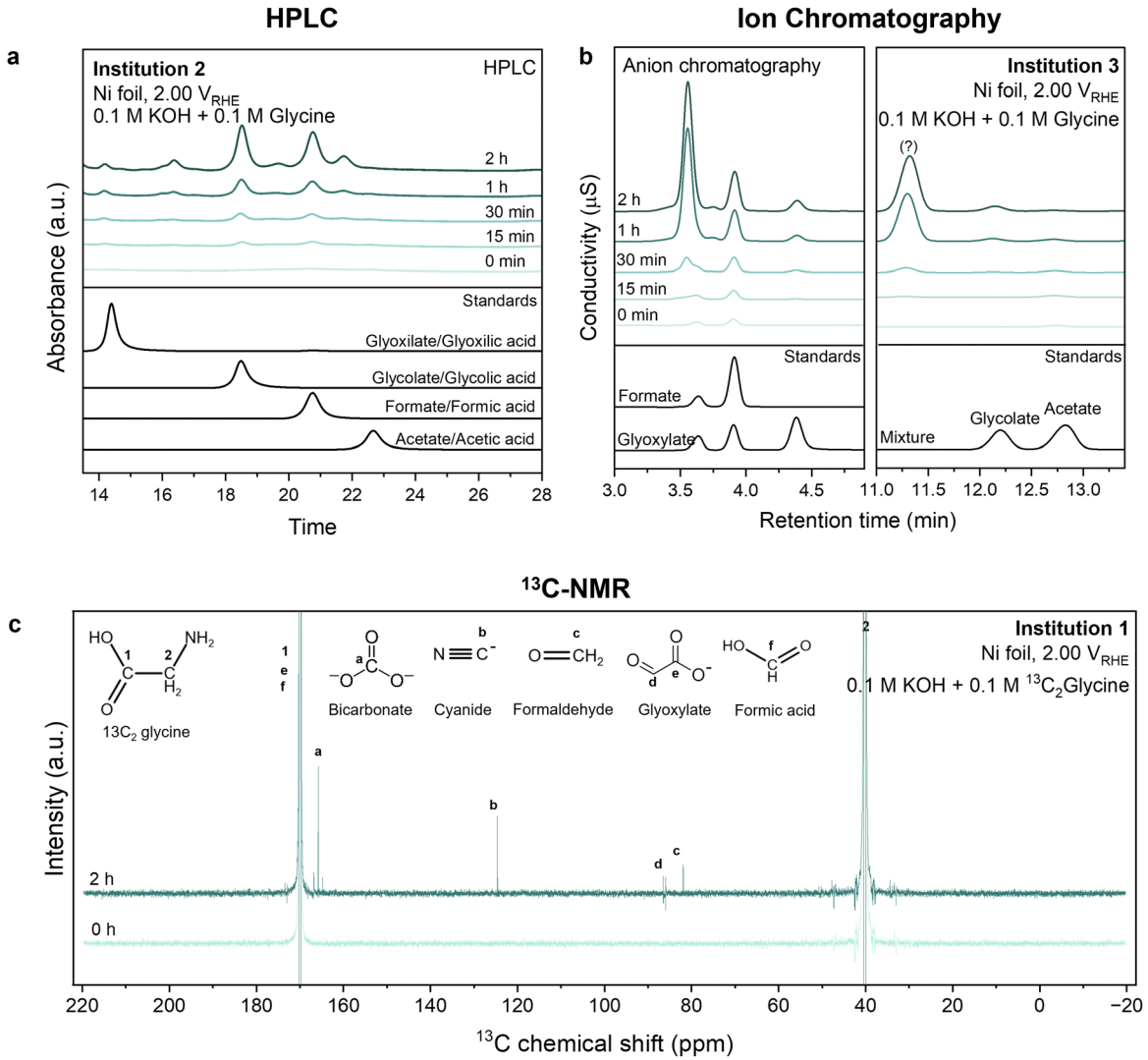

Fig. 2 Characterization of carbon byproducts during electrochemical glycine oxidation on Ni at 2.00 V_{RHE}. (a) HPLC of electrolyte solutions at increasing reaction time up to 2 h. Carbon product standards are shown in the lower panel. (b) Anion chromatography spectra of electrolyte solutions undergoing electrochemical glycine oxidation at increasing time stamps up to 2 h. The glycolate-acetate detection (right panel) has been specifically conducted at a higher column temperature to separate these peaks, which would otherwise overlap at room temperature (see SI). (c) ^{13}C-NMR spectra of glycine electro-oxidation using $^{13}C_2$ glycine, where products such as carbonate, cyanide, formaldehyde, glyoxylate and formic acid appeared after 2 h of electrolysis. The experimental condition corresponds to the benchmarking condition of Ni electrode at 2.00 V_{RHE} as described in Fig. 1.

electrochemical glycine oxidation at 2.00 V_{RHE} (Fig. 3a). The detection of an N-containing C_1 intermediate (*i.e.*, CN^-) implies that the initial step of glycine activation may involve direct C–C bond cleavage, consistent with pathway 1 (Fig. 3a, top). Through this pathway, glycine could be converted to methylamine (CH_3NH_2), which may subsequently transform into formaldehyde and ammonia *via* a CN^- intermediate. This intermediate is supported by previous *in situ* spectroscopy studies, where surface-bound *CN- and *CNO- were identified on Pt[24] and Au[25] based on the peak location and the Stark shifts. However, the direct C–C bond cleavage in glycine necessary to form methylamine requires a two-electron reduction of glycinate (the deprotonated form of glycine) *via* $NH_2CH_2COO^- + 2H_2O + 2e^- \rightarrow CH_3NH_2 + 2OH^- + HCOO^-$, which may be unfavorable under strongly oxidative conditions. Nevertheless, methyl-, dimethyl-, and trimethylamine have been detected in previous work, including during electrolytic oxidation of α-amino acids in acid on PbO_2 by Takayama *et al.*[21] and during glycine oxidation at pH 13 on Pt reported by Maragoni *et al.*,[21] suggesting that the formation of methylamine can occur despite oxidizing electrode potentials, potentially *via* coupled oxidation–reduction processes. Methylamine, which would lead to CH_4N^+ fragments at m/z = 30, was not detected in this work (Fig. S18), potentially due to its fast conversion to other products, including CN^-, which was detected as a prominent reaction product (Fig. 2c) from oxidative transformation of methylamine to CN^-. Once formed, CN^-, being hydrogen-deficient, could undergo further oxidation to cyanate (CNO^-),

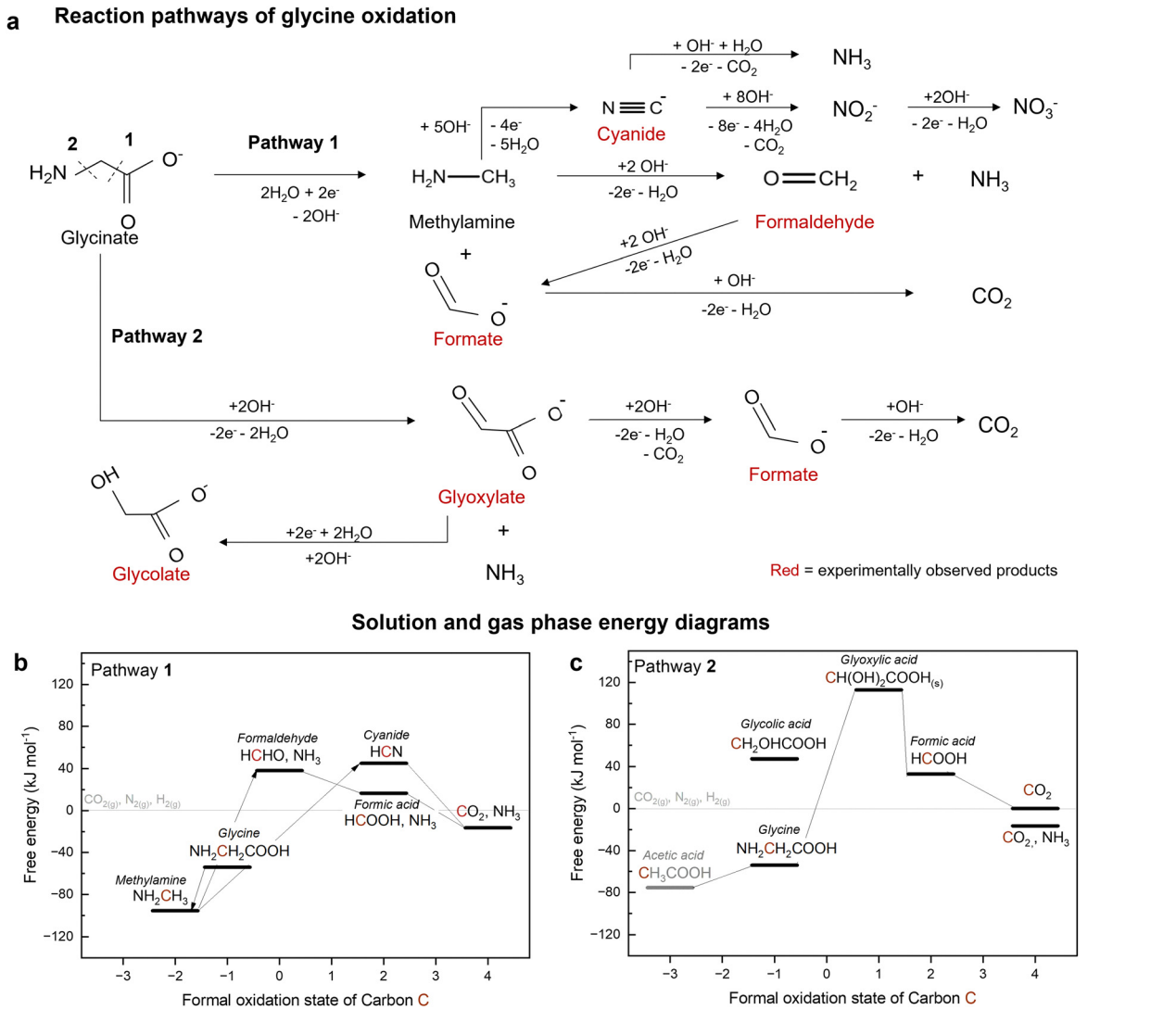

Fig. 3 Reaction pathways during electrochemical glycine oxidation. (a) Proposed reaction pathways based on the detected reaction products, denoted in red as characterized in Fig. 2. Free energy diagrams of the pure phases with increasing oxidation state of the carbon are depicted for pathway 1 (b) and pathway 2 (c) based on the available thermodynamic data. All species and reactions are expressed in their protonated form and used the standard free energy of formation of the pure phases: crystalline solids for glycine, glyoxylic acid (*i.e.* in its hydrated form, dihydroxyacetic acid) and glycolic acid; liquids for acetic acid, formic acid, cyanic acid (HCN); gases for formaldehyde, methylamine, CO_2, NH_3 and H_2. Formal oxidation states were assigned using the ionic approximation by attributing bonding electrons to the more electronegative atom, and the resulting charge defines the oxidation state. Zero free energy corresponds to $CO_{2(g)}$, $NH_{3(g)}$, $H_{2(g)}$ at 1 bar and 298 K. Full chemical equations and the reaction free energy calculations can be found in Table S3.

nitrite (NO_2^-), and nitrate (NO_3^-) which has been reported to occur electrochemically on a copper-complex at 0.75 V *vs.* Hg/HgO at pH = 12 ($\sim$1.5 V_{RHE}),[46] suggesting CN^- as a selectivity marker favoring NO_x formation over NH_3. Alternatively, sequential protonation of nitrogen coupled with C–N bond cleavage could lead to ammonia formation $CN^- + OH^- + H_2O \rightarrow NH_3 + 2e^- + CO_2$, consistent with prior reports of ammonia production from cyanide using Ti/SnO_2-based anodes.[47] Further studies are needed to elucidate the electrochemical oxidation of CN^- to form NH_3 *vs.* NO_x.

Alternatively, the existence of C_2 products that do not contain nitrogen, such as glyoxylate ($OCH–COO^-$) and glycolate ($HOCH_2COO^-$) suggests that direct C–N bond cleavage to liberate ammonia occurs on Ni, as depicted in pathway 2 (Fig. 3, bottom). In this route, glycine is oxidized directly to glyoxylate ($OCH\text{-}COO^-$) and ammonia according to $NH_2CH_2COO^- + 2OH^- \rightarrow OCH–COO^- + NH_3 + H_2O + 2e^-$ and the carbon in glyoxylate is further oxidized to formate and ultimately CO_2. Interestingly, glycolate likely comes from two-electron reduction of glyoxylate, which is commonly observed in biological systems through glyoxylic acid reductase (GAR).[48] Thus, its presence at 2.00 V_{RHE} may imply a coupled oxidation–reduction process occurring on Ni, which warrants further investigation. Overall, glycine activation *via* either C–C cleavage (pathway 1) or C–N cleavage (pathway 2) appears to be feasible during electrochemical oxidation on Ni, but the extent of the two pathways requires consideration of the reaction energetics.

We further discuss the feasibility of different mechanisms by examining the thermodynamic stability of the reaction intermediates using the gas or solution phase free energies (Fig. 3b and c). We note that the bulk thermodynamic values do not include surface adsorption or electric field effects prominent in electrochemical reactions on a heterogeneous surface, but can provide a starting point in understanding the relative stability of reaction intermediates. Such thermodynamic analysis indicates that both pathways involve a similarly uphill step, and that C–N bond cleavage is generally the most energetically uphill step. Using standard Gibbs formation energies for carbon-containing species (Table S3), the energy diagram for pathway 1 (Fig. 3b) shows that the conversion of methylamine to formaldehyde and ammonia, $CH_3NH_{2(g)} + 2OH^- \rightarrow CH_2O_{(g)} + NH_{3(g)} + 2e^- + H_2O_{(l)}$ is the most uphill step, with ΔG_r = +133.0 kJ mol^{-1}. The subsequent oxidation of formaldehyde to formic acid and CO_2 is energetically downhill. When cyanide is considered as an intermediate, its formation from methylamine $CH_3NH_{2(g)} + 5OH^- \rightarrow HCN_{(l)} + 2e^- + H_2O_{(l)}$ is the most uphill step (ΔG_r = 140.5 kJ mol^{-1}), while further oxidation to NH_3 and CO_2 is thermodynamically favorable. The experimental observation of CN^- as a prominent byproduct is at odds with the thermodynamic analysis, indicating that kinetic barriers on the surface or other surface thermodynamic reaction steps should be considered. For pathway 2 (Fig. 3c) involving sequential oxidation of glycine to glyoxylic acid, formic acid, and CO_2, glycine oxidation to glycolic acid *via* $NH_2CH_2COOH_{(s)} + 2H_2O_{(l)} \rightarrow CH(OH)_2COOH + NH_3 + 2H^+ + 2e^-$, ΔG_r = +150.4 kJ mol^{-1}, is the most uphill step. The subsequent oxidation steps of carbon from glyoxylic acid to ultimately CO_2 appears to be strongly downhill. This analysis supports C–N bond cleavage as the rate-determining step. However, capturing the true rate-limiting steps and reaction selectivity will require a detailed investigation of charged species adsorption (*e.g.*, glycinate/carboxylate species and CN^-). This will involve grand-canonical density functional theory and microkinetic modeling, supported by experimental probes such as kinetic isotope effects and Tafel slope analysis, and is the subject of future work.

We consider several hypotheses regarding the origin of the oxidizing species responsible for glycine oxidation on the Ni surface. One possibility is oxidation mediated by NiOOH formed through the Ni^{2+}/Ni^{3+} redox transition,[49,50] described by $Ni(OH)_{2(s)} + OH^-_{(aq)} \rightarrow NiOOH_{(s)} + H_2O_{(l)} + e^-$. NiOOH can therefore act as a primary oxidant, which has been demonstrated for the electrochemical oxidation of urea[27,37] and alcohols.[28] This hypothesis is supported by the fact that glycine oxidation to ammonia occurs at potentials >1.60 V_{RHE} (Fig. 1d), which are well above the Ni^{2+}/Ni^{3+} redox transition at $\sim$1.35 V_{RHE}.[51] Alternatively, the formation of surface NiO_x species may enable the generation of reactive oxygen species such as peroxide and superoxide species, with prior studies indicating that hydroperoxides[52] and $OH^\bullet$ radical,[53] such as those generated *via* Fenton chemistry, can oxidize amino acids. Another possibility involves singlet oxygen ($^1O_2$), a highly reactive oxidant that can arise from spin-conservation constraints during oxygen evolution and then decay to triplet oxygen ($^3O_2$). The generation of $^1O_2$ has been reported on Ni-based cathodes,[54] where it induces severe oxidative decomposition of aprotic solvents to generate carbon-byproducts such as Li–acetate, Li–formate and Li_2CO_3 that severely limit the cyclability of Li-ion and Li–O_2 batteries,[54] and is thermodynamically accessible with a calculated reversible potential of 1.475 V_{RHE} for $2H_2O \rightarrow {}^1O_2 + 4H^+ + 4e^-$.[55] Interestingly, these aprotic byproducts are structurally similar to glycinate (structurally equivalent to acetate but with an -NH_2 group substituted onto the methyl carbon), formate and CO_3^{2-} detected in this work (Fig. 2), hinting at $^1O_2$ as a possible oxidant assuming similar reactivity in protic environments. Further mechanistic studies are therefore required to identify the dominant oxidizing species responsible for glycine activation, which will inform future catalyst design aimed at decoupling oxidant generation from electrode corrosion.

Assessing the influence of experimental conditions on product selectivity

Given the diversity of reaction products from glycine oxidation and motivated by the challenges in benchmarking the nitrogen selectivity across institutions (Fig. 1), we investigated the effect of several experimental parameters such as stirring, electrode area size, and cell design (Fig. 4). In addition to N selectivity, their influence on the selectivity to carbon byproducts is also particularly discussed to allow interpretation of mechanistic implications. At institution 3, the benchmarking condition that yielded an ammonia Faradaic efficiency of $\sim$26% corresponded

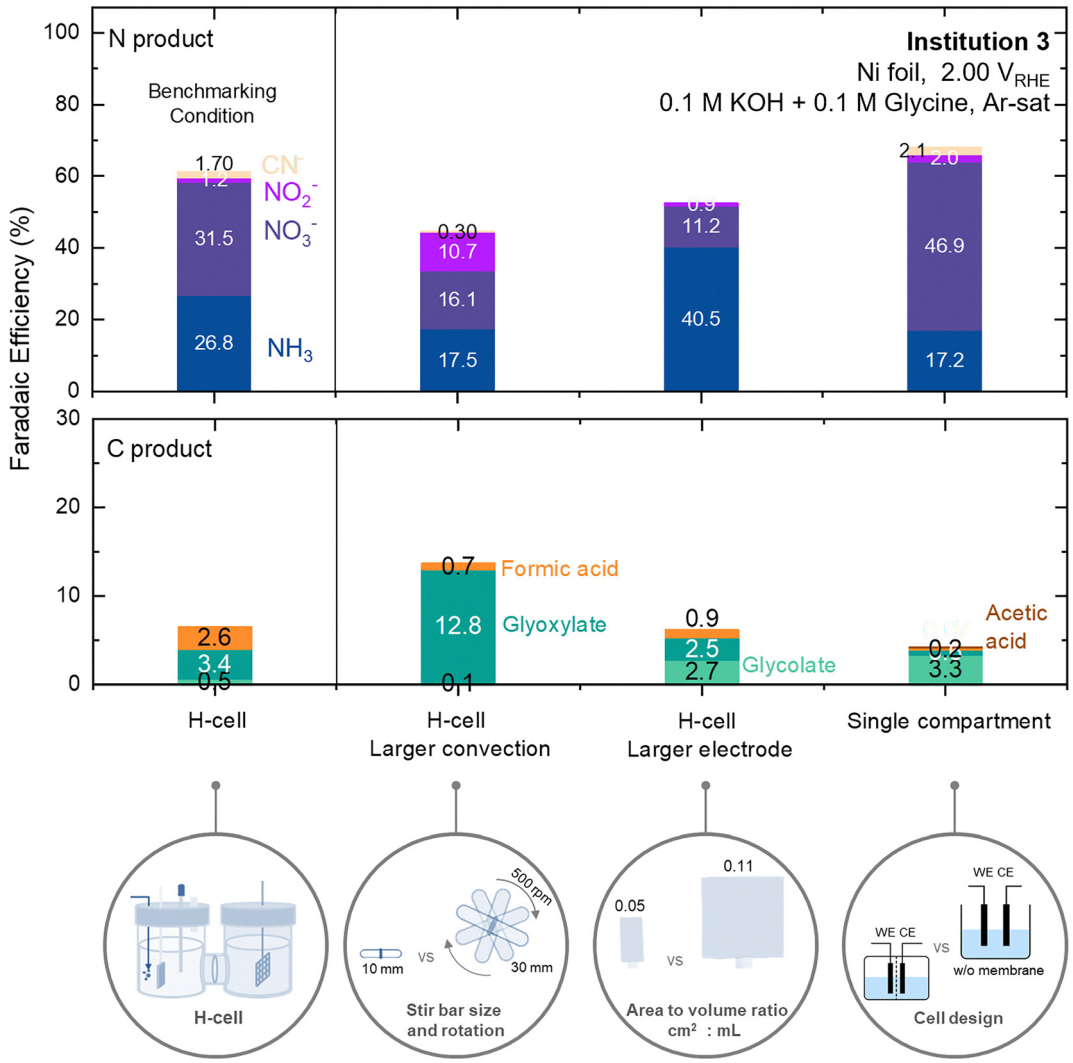

Fig. 4 Effect of experimental design on the nitrogen and carbon products of electrochemical glycine oxidation on Ni. The benchmarking condition (most left) corresponds to conditions described in Fig. 1, using an H-cell containing an anion-exchange membrane and micro stir bar (10 mm) rotated at 300 rpm. The faradaic efficiencies from experiment 3–1 from institution 3 has been plotted (see Table S1) as the carbon product quantification is available for this experiment. Relative to the benchmarking condition, three changes of experimental conditions have been investigated: larger convection *via* higher rotation of a larger stir bar, larger electrode area and undivided compartment (*i.e.* single cell) in lieu of H-cell, showing significant influence of these factors on the production and distribution of the N- (top panel) and C-based (bottom panel) products. The faradaic efficiency calculation for NH_4^+, NO_3^-, NO_2^- and CN^- and for glycolate, glyoxylate and formic acid can be found in Experimental section.

to a relatively static electrolyte without stirring, which more closely resembled the conditions at institutions 1 and 2, where a small (10 mm) stir bar was used. The overall FE to these carbon byproducts amounted to 6% (Fig. 4, bottom), which represents ~20% of the carbon balance while the remaining ~80% was attributed to CO_2 (Fig. S33). Institution 3 first conducted electrolysis using a larger 30 mm magnetic stir bar operating at 500 rpm. Increased convection led to a pronounced decrease in ammonia Faradaic efficiency from 26.8% to 17.5%. Faradaic efficiencies toward NO_2^- and NO_3^- also slightly decreased under stirring, with their combined contribution decreasing from ~32% under static conditions to ~27%, while the relative proportion of NO_2^- increased with stronger convection. Accordingly, the higher NO_2^- observed at institutions 1 and 2 (~10–16%) compared to institution 3 during benchmarking (Fig. 1b) may be attributed to an intermediate degree of convection (1.0 mm stir bar at 300 rpm), lying between static and strongly convective conditions explored at institution 3 (Fig. 4a, first two columns). Taken together, these observations suggest several mechanistic implications: First, although increased convection would be expected to reduce ammonia residence time near the electrode surface and suppress its further oxidation, ammonia faradaic efficiency decreased without a corresponding increase in NO_2^-/NO_3^-, indicating that oxidized nitrogen species likely originate from direct amine oxidation rather than the oxidation of produced ammonia. Second, the enhanced formation of glyoxylate under larger convection (FE = 12.8% *vs.* 3.4%), concurrent with suppressed ammonia and formate production, suggests that glycine

activation *via* C–N cleavage (pathway 2, Fig. 3a) was favored by convection but less effective at producing ammonia than pathway 1, in which ammonia and formate are generated *via* a methylamine intermediate (Fig. 3a). Future work is needed to quantitatively resolve the influence of mass transport on product selectivity.

The effect of electrode surface area was investigated by doubling the electrode area while keeping the same electrolyte volumes in both compartments (*i.e.* 0.05 to 0.1 cm_{geo}^2: mL ratio), with no stirring. Increasing the electrode area led to a substantial enhancement in ammonia Faradaic efficiency, from ~26% to ~40% (Fig. 4, top). In contrast, the faradaic efficiency toward NO_3^- decreased markedly from 31.5% to 11.2% with the larger electrode. The carbon product distribution also exhibited discernible changes, with glycolate Faradaic efficiency increasing to 2.7% for the larger electrode compared to 0.5% at benchmarking (Fig. 4, bottom). Taken together, these results indicate that a larger electrode area favors ammonia production, potentially by enabling a greater extent of coupled oxidation–reduction processes at the electrode surface when the oxidative potential 2.00 V_{RHE} was applied. In this context, both methylamine formation from glycine and glycolate formation from glyoxylate involve reductive steps (Fig. 3a), which may benefit from increased electrode area. These findings also suggest that reactor design and optimization of mass transport is critical in controlling the activity and selectivity of practical amino acid electrolysis. Finally, the influence of cell design was evaluated by comparing the H-cell configuration (*i.e.* the benchmarking condition) with a single-compartment/undivided cell, while keeping the electrode area-to-volume ratio (*i.e.* 0.05 cm_{geo}^2: mL) the same without stirring. The undivided cell produced an overall Faradaic efficiency for nitrogen-containing products (NH_3, NO_3^-, NO_2^-, and CN^-) of 66.1%, comparable to the benchmark H-cell value of 63.2%, but with a larger fraction of NO_3^- relative to NH_3 (Fig. 4, top). In addition, glycolate Faradaic efficiency increased to 3.3% from 0.5% in benchmarking condition (Fig. 4, bottom). This shift in selectivity may be linked to the pH drop during electrolysis: during the benchmarking H-cell conditions with an anion-exchange membrane, the working electrode compartment experienced a larger pH drop ($\Delta pH \approx -0.5$) compared to the undivided cell ($\Delta pH \approx -0.2$, see Fig. S34 and Table S4). These observations suggest that electrolyte pH may influence glycine oxidation pathways and the resulting ammonia and carbon product selectivity, warranting further investigation.

Impact of potential pulsing on ammonia efficiency

Recognizing the benefits of dynamic electrocatalysis *via* potential pulsing, the effects of pulsing are herein investigated, with particular emphasis on how the resulting Faradaic efficiencies differ from those obtained under constant potential. Three potential pulses were investigated and compared to the 'benchmarking' constant potential experiment at 2.00 V_{RHE} (Fig. 5a). A symmetric 5 s hold at the positive and negative potentials was selected based on timescales over which pulsing effects have been reported in other electrochemical reactions,[30,31] providing a reasonable starting point. For pulsing 1–3, progressively higher positive potentials were applied (Fig. 5b–d). The raw negative potential (prior to *iR* correction) was kept constant and sufficiently negative (< -0.10 V_{RHE}) to promote surface *H coverage on Ni,[56] which may be important in facilitating hydrogenation of amine to ammonia. After *iR* correction, however, the negative potential varied within ±~20 mV due to fluctuations in the recorded current (Fig. 5b–d). Several observations emerge from the electrochemical profiles. First, the working electrode potentials after iR correction during pulsing showed considerably larger variations compared to constant-potential electrolysis. The stabilized positive potentials, obtained by averaging the final 1 s of each 5 s pulse (Fig. S38–S40), were 1.65 V_{RHE} ± 7 mV (Fig. 5b and e) 1.78 V_{RHE} ± 17 mV (Fig. 5c and f) and 1.83 V_{RHE} ± 67 mV (Fig. 5d and g). However, when the whole 5 s is considered (excluding the first 0.1 s from capacitive contributions), *iR*-corrected potential variation during the positive pulse increased to ~60 mV, ~100 mV and ~400 mV for pulsing 1, 2, and 3 respectively (Fig. S35–S37). Second, differences were observed in the current–time profiles. For pulsing 1 and 2, the positive pulses showed the conventional behavior of a high initial current decaying to a steady state (Fig. 5e and f), consistent with a transition from capacitive to faradaic currents. In contrast, pulsing 3 exhibited a more rounded/unusual initial response (Fig. 5g and Fig. S37). Analysis of the raw (uncorrected) potential indicates that this arises from a longer time (~0.5 s) required for the potential to reach its set value (Fig. S40), likely due to potentiostat overload at high potentials, which limits accurate capture of currents at the initial stages. These observations underscore the importance of improved cell designs with reduced solution resistance for accurate high-potential pulsing studies.

Ammonia Faradaic efficiency (FE) with pulsing generally shows a significant improvement relative to constant-potential electrolysis, yet the magnitude of this enhancement is highly sensitive to how the Faradaic charge is accounted for (Fig. 5h). The constant-potential experiment yielded an ammonia FE of 18.4 ± 0.9% over 1 h across three independent repeats. Notably, the same experiments produced an FE of 23.8 ± 1.0% over 2 h (Table S1), consistent with cross-institution benchmarking results (Fig. 1), indicating higher efficiency at longer electrolysis times. In calculating the FE from pulsing experiments, three accounting methods were used to determine the total Faradaic charge (Q_{total}): (i) summing positive and negative charges with their signs preserved (Fig. 5h, left), (ii) considering only the positive charge (Fig. 5h, middle), and (iii) summing the absolute values of positive and negative charges (Fig. 5h, right). When method (i) is considered, serving as the most 'optimistic' estimate of the Faradaic efficiency, pulsing 1 and 2 yield substantially higher ammonia FEs of up to ~80%. In contrast, when negative charge contributions are excluded or counted in absolute terms (methods ii and iii), the calculated FEs decrease markedly and converge toward those obtained under constant-potential conditions. The sensitivity of FE to charge accounting is most pronounced for pulsing 1 (Fig. 5b and e), where the total positive charge

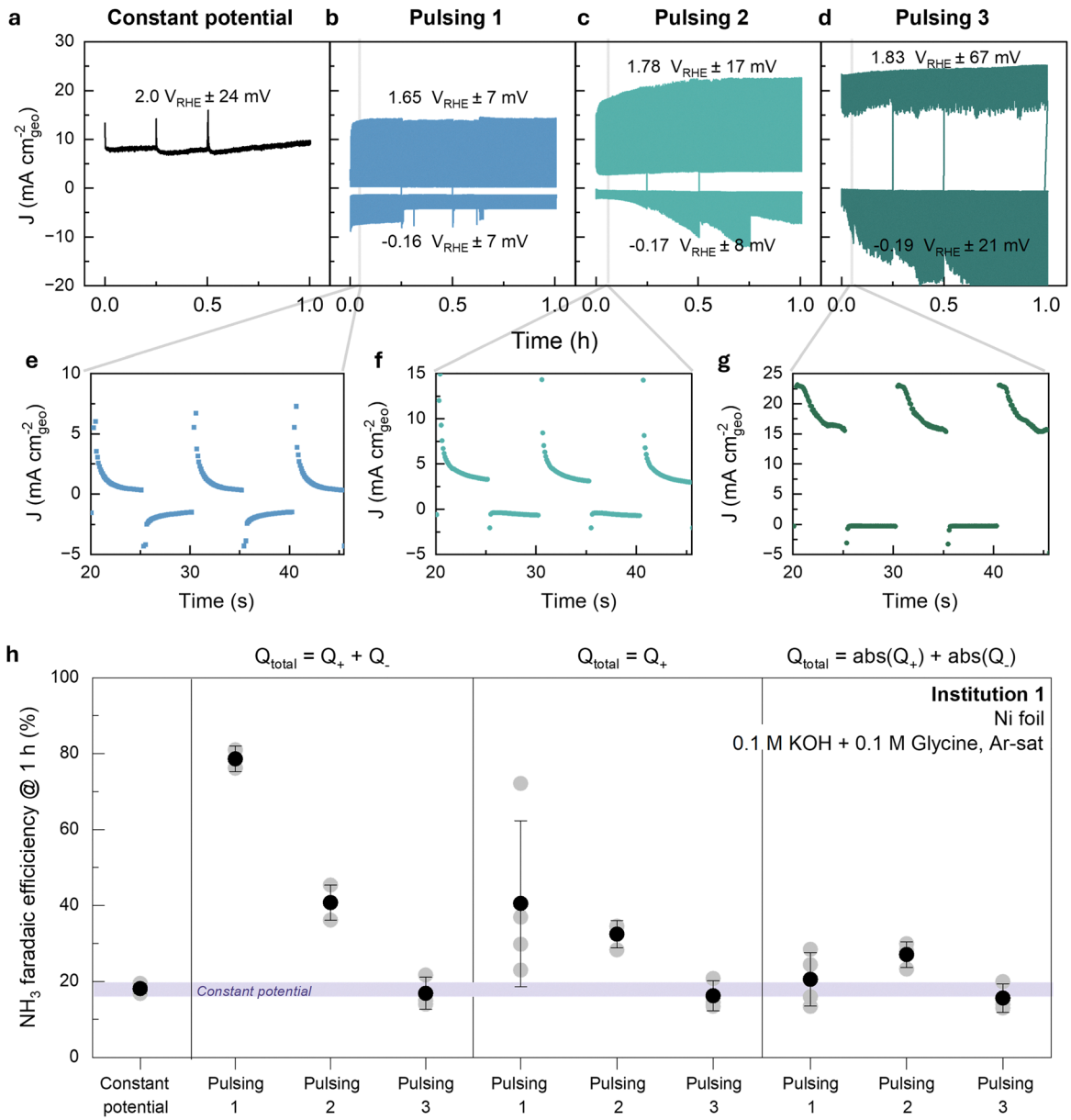

Fig. 5 Investigating the impact of potential pulsing on NH_3 efficiency. (a) Chronoamperometry profile of electrochemical glycine oxidation with polished Ni at 2.00 V_{RHE} 0.1 M KOH + 0.1 M glycine (Ar-sat) over 1 hour, corresponding to the 'benchmarking condition' outlined in Fig. 1. (b)–(d) Electrochemistry profile of three pulsing conditions at increasing values of the positive potentials from +1.65 V_{RHE} (pulsing 1, b), 1.78 V_{RHE} (pulsing 2, c) and 1.83 V_{RHE} (pulsing 3, d), while the negative potential values are kept nominally similar but showed differences in currents resulting in differences in *iR*-corrected potentials. Zoomed-in view of the current profiles are shown in panels e, f and g for pulsing 1, 2 and 3 respectively, where the positive and negative potentials were held for 5 s. The average and standard deviation of the potentials are determined from the last 1 s of the 5 s pulse (see Fig. S38–S40 for demonstration), during which the current is stable, over the entire 1 h duration and across 3 independent repeats. (h) NH_3 faradaic efficiency comparison between the constant potential experiments at 2.00 V_{RHE} and the pulsing experiments with three different methods of charge accounting: the sum of positive and negative charges (left), the positive charges only (middle) and the absolute values of the positive and negative charges. The faradaic efficiency to ammonia, calculated assuming $z_{e^-} = 6$ from $NH_2CH_2COOH + 2H_2O_{(l)} \rightarrow NH_{3(g)} + 2CO_{2(g)} + 6(H^+ + e^-)$, see Table 2. Error bars indicate $n \geq 3$ independent measurements (see Tables S5 and S6 for the tabulated results).

passed is the lowest in magnitude and at levels comparable to the negative charge (Table S5). In addition, the FE from pulsing experiments exhibit generally larger error bars, which we attribute to the greater variation of the working electrode potential associated with *iR*-correction. Despite these variations, the enhancement in FE relative to constant-potential electrolysis remains robust beyond experimental uncertainty. In particular, pulsing 2, which employs a lower positive potential of 1.78 $V_{RHE} \pm 17$ mV, delivers at least ~10% higher ammonia FE (~30% as the lower bound) than the static experiments at 2.00 V_{RHE} (Fig. 5h, right) regardless of the accounting methods used.

The enhancement in ammonia FE *via* pulsing suggests several mechanistic implications. The effectiveness of pulsing to the *H coverage regime (<-0.1 V_{RHE} on Ni[56]) implies that the rate-limiting step of C–N bond cleavage, which we hypothesized in accordance with the thermodynamic analyses in Fig. 3, is linked to the hydrogenation of the amine group to form ammonia. At oxidative potentials, hydrogen availability is limited because water preferentially undergoes oxidation to O_2 and H^+ above 1.23 V_{RHE}. Pulsing to negative potentials may therefore transiently increase *H coverage, facilitating amine hydrogenation and C–N bond cleavage. Alternatively, the benefit of pulsing may arise from active-site regeneration. In this case, cycling the potential enables repeated Ni^{2+}/Ni^{3+} redox transitions, regenerating NiOOH as the active oxidizing species and sustaining the conversion. The sensitivity of pulsing results highlights the need for clear charge accounting and further mechanistic investigation to elucidate the contributions of positive and negative charge toward ammonia production. Nevertheless, these results highlight opportunities to optimize pulsing conditions to enhance ammonia efficiency while reducing anodic overpotential, which should ultimately align with the practical energy efficiency targets defined by future technoeconomic analyses.

Extending mechanistic insights to other amino acids

Given the diversity of amino acids and their compositions in activated waste sludge (see Table 1), we expand the electrochemical characterization to assess the applicability of insights derived from glycine to other amino acids. As an initial library, alanine, lysine, and aspartic acid were selected to represent a range of side groups: alanine with a simple methyl group at the α-carbon, lysine with a side chain containing an additional amine, and aspartic acid with a carboxylic acid side group. Similar to glycine, electrochemical oxidation of these amino acids in alkaline electrolyte on Ni foil at 2.00 V_{RHE} yielded NH_3 as the dominant nitrogen product (Fig. 6a), accounting for 90%, 85%, and 85% of the total nitrogen for alanine, lysine, and aspartic acid, respectively. The remaining nitrogen balance is attributed to NO_3^- and NO_2^-, while no gas-phase nitrogen products such as N_2 and NO were detected (Fig. S41–S43). Similar to glycine, the production of the ammonia-dominated product is accompanied by appreciable Ni dissolution (Fig. S44) albeit by different amounts, in the order of glycine (53.4 μmol ± 44.5 over the 2 h electrolysis) > alanine (16.1 umol) > lysine (0.1 umol) > aspartic acid (0.1 umol), which significantly exceeded that in the absence of amino acids (*i.e.* OER in 0.1 M KOH, Fig. S27). Charge balance was assessed by computing the FE associated with the observed products (NH_3, NO_3^-, NO_2^-, Ni^{2+} and O_2), assuming full oxidation of C to CO_2. The ammonia FE follow a similar ranking in the order of alanine (FE_{NH_3} = 63.5% assuming z_{e^-} = 12) > lysine (FE_{NH_3} = 45.4%, z_{e^-} = 14) > glycine (FE_{NH_3} = 23.7% ± 1.8, z_{e^-} = 6) > aspartic acid (FE_{NH_3} = 10.9%, z_{e^-} = 12, see Table S1). We note that the cumulative FE of glycine and aspartic acid including products from NH_3, NO_3^-, NO_2^-, Ni dissolution and O_2 evolution, reaches 100% within experimental uncertainty (Fig. S44), thereby closing the charge balance. On the other hand, those for alanine and lysine exceed unity by ∼20%, which might suggest that the carbons were not fully oxidized to CO_2, thereby resulting in the lower actual z_{e^-} values than z_{e^-} = 12 and z_{e^-} = 14, respectively. Overall, screening of additional amino acids reveals a consistent trend of ammonia as the dominant nitrogen-containing product, accompanied by appreciable Ni dissolution. Meanwhile, variations in ammonia efficiency highlight the strong influence of side-chain character in governing amino acid oxidation.

We correlate ammonia production with competing processes and side-chain character to probe the mechanism of ammonia generation during amino acid oxidation. In lieu of FE, the product converted in moles normalized to the total charge passed (in units of mol of products per coulomb of passed charge, $\mu mol_{prod}\ C^{-1}$), denoted as the charge efficiency to the product, has been used to avoid ambiguity in the number of electrons z_{e^-}. Firstly, increasing charge efficiency toward ammonia was linearly correlated with decreasing charge efficiency to O_2 (Fig. 6b), indicating that O_2 is parasitic to ammonia production. Mechanistically, this correlation supports the hypothesis that both processes share a common active site. In this context, NiOOH associated with the Ni^{2+}/Ni^{3+} transition is known to be key for O_2 evolution activity[51,57] but may also competitively act as the primary oxidant for amino acid conversion to ammonia. Secondly, the charge efficiency to ammonia correlated approximately logarithmically with increased Ni dissolution (Fig. 6c). This observation supports the hypothesis that dissolved Ni plays an active role in thermodynamically stabilizing ammonia, such as *via* the Ni–NH_3 complex. Another hypothesis consistent with this observation is that Ni^{2+} may kinetically accelerate amino acid decomposition *via* redox mediation: initial Ni^{2+}-amino acid complexation followed by oxidation to Ni^{3+} by the electrode generates a solution-phase oxidant that promotes oxidative deamination, releasing ammonia.[58,59] We further examine the relationship between Ni^{2+} dissolution and side-chain character. Previous computation[60] has shown that aspartic acid binds Ni^{2+} much more strongly ($E_{binding}$ = ∼350 kJ mol^{-1}) than other amino acids ($E_{binding}$ = ∼250 kJ mol^{-1} for glycine, alanine and lysine) due to its two negatively charged carboxyl groups. However, the Ni^{2+} dissolution in aspartic acid (0.003 $\mu mol_{Ni}\ C^{-1}$) is the lowest among the amino acids studied. This result suggests that the Ni electrode instability in the presence of amino acids stems not from the parasitic Ni^{2+}-amino acid coordination, but instead actively facilitates ammonia formation *via* nickel complexation, which improves the thermodynamic stability of ammonia and reaction intermediates and concurrently lowers kinetic barriers. Thirdly, increasing charge efficiency to ammonia is associated with increasing $NO_{2/3}^-$ (Fig. 6d). This result supports the hypothesis that NH_3 and $NO_{2/3}^-$ production are bottlenecked by a common rate-limiting step of C–N cleavage (see Fig. 4b and c). Based on these correlations, we hypothesize that the electrochemical activity for amino acid activation can be rationalized by the side-chain character (see top of Fig. 6). (i) Glycine and alanine, with simple side

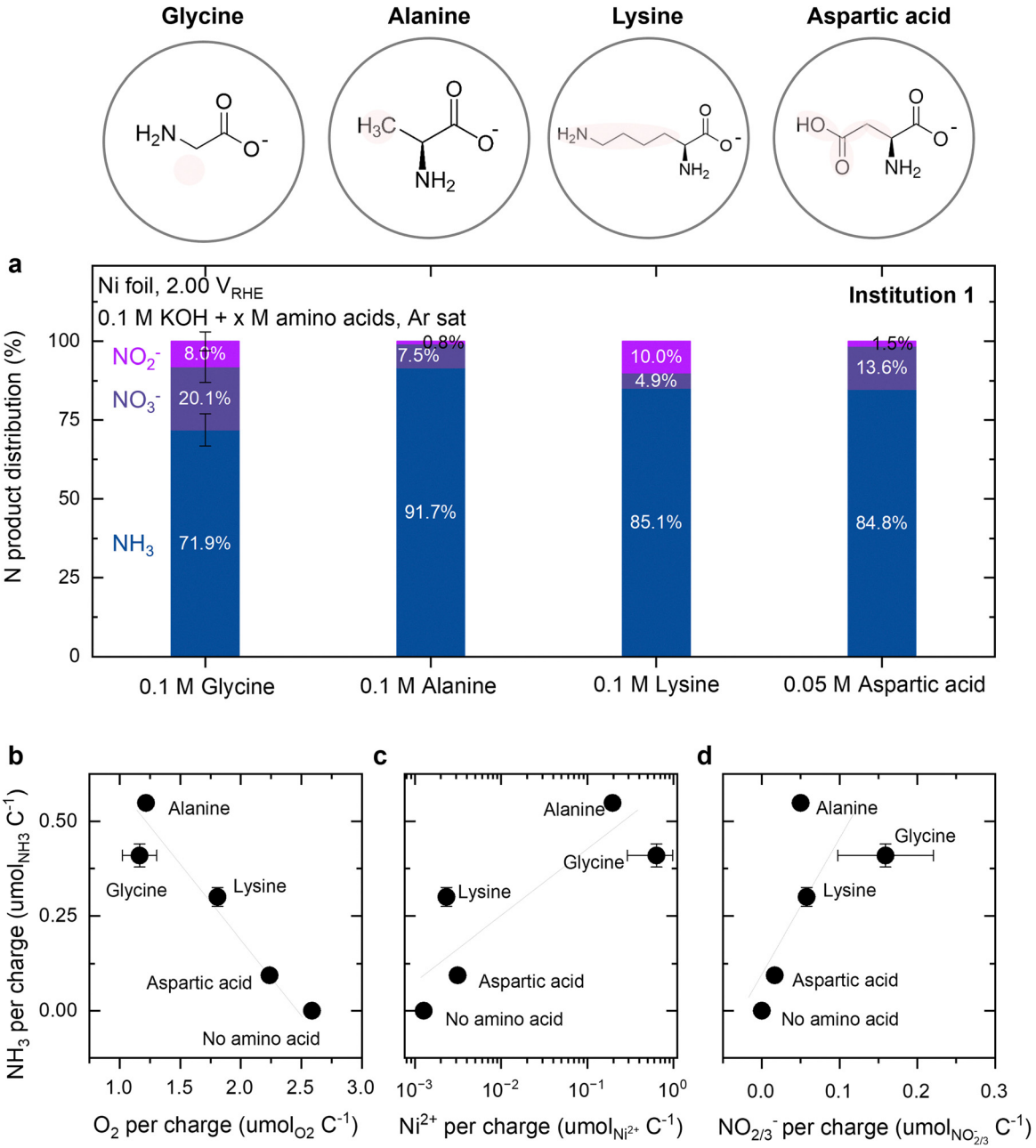

Fig. 6 Evaluating electrochemical oxidation of different amino acids. (a) Nitrogen product distribution (NH_3, NO_3^- and NO_2^-) from the electrochemical oxidation of glycine, alanine, lysine and aspartic acid in 0.1 M KOH with Ni foil in an H-cell. The molecular structures of the amino acids are displayed above. All experiments were conducted by institution 1. The chronoamperometry profiles and quantification of gas and solution-phase products are shown in Fig. S41–43 and Table S1, respectively, where the average iR-corrected potentials over 2 hours were measured to be 1.98 ± 0.025 V_{RHE}, 2.04 ± 0.030 and 2.03 ± 0.007 for Alanine, Lysine and Aspartic acid respectively. (b)–(d) Correlations between the charge efficiency towards ammonia production and towards O_2 evolution (b), Ni dissolution (c) and $NO_{2/3}^-$ production (d). Data correspond to electrochemical oxidation of the four amino acids in alkaline electrolytes on Ni foil at 2.00 V_{RHE} are shown, while the 'no amino acid' case represents 0.1 M KOH. For the "no amino acid" case, the charge efficiency associated with Ni dissolution was calculated from measured Ni^{2+} concentrations (Fig. S27, institution 1). The remaining charge was attributed to O_2 evolution, as no NH_3 or $NO_{2/3}^-$ formation is expected in the absence of amino acids. Error bars represent standard deviation from up to n = 7 and n = 2 for glycine and lysine, respectively.

groups, exhibit higher NH_3 and NO_x efficiencies, likely due to higher surface coverage of amino acid adsorption. (ii) Lysine shows moderate efficiencies, where the longer side chain may reduce adsorption coverage despite the additional amine. (iii) Aspartic acid exhibits the lowest efficiencies, due to alternative COO^--down adsorption[25] on the positively charged Ni surface from the carboxylate side-group rather than the α-functional group. While further work is needed to quantitatively link charge efficiency with broader amino acid structures, these results provide insight into the origin of ammonia production

and its dissolution-mediated mechanism under oxidative potentials.

Recommended practices for reporting of electrochemical amino acid conversion for ammonia recovery

Given the significant influence of the experimental parameters identified in this benchmarking effort, an experimental protocol (grey), together with additional considerations (blue), is proposed in Fig. 7. Prior to experimentation, a consistent preparation procedure, comprising thorough cell cleaning and electrode polishing with freshly prepared electrodes for each experiment, is recommended to ensure reproducible conditions and to prevent contamination from previous runs. Particular attention should be paid to the reference electrode, which should be calibrated with respect to the electrolyte of interest to enable reliable comparison across experiments. During electrolysis, several diagnostic checks, such as cyclic voltammetry and solution resistance measurements *via* electrochemical impedance spectroscopy, can help ensure reproducible performance by identifying issues related to electrode and electrolyte quality, as well as cell-assembly parameters such as electrode spacing. We also emphasize the importance of reporting iR-corrected potentials, noting that the resistance term R can meaningfully depend on cell geometry and assembly. More importantly, as demonstrated in the experimental assessment in Fig. 4, parameters related to convection (*e.g.*, stir bar size and rotation rate, gas bubbling) and electrode dimensions (*e.g.*, area-to-volume ratio) should be fully reported.

For product quantification, we caution against the use of colorimetric methods for ammonia, nitrate/nitrite, and carbon product detection, as these techniques were shown to suffer from interferences arising from amino acids, metal ions, and reaction byproducts (see the Experimental section). In contrast, ^{1}H NMR spectroscopy and ion chromatography were found to be reliable when implemented with consistent sample

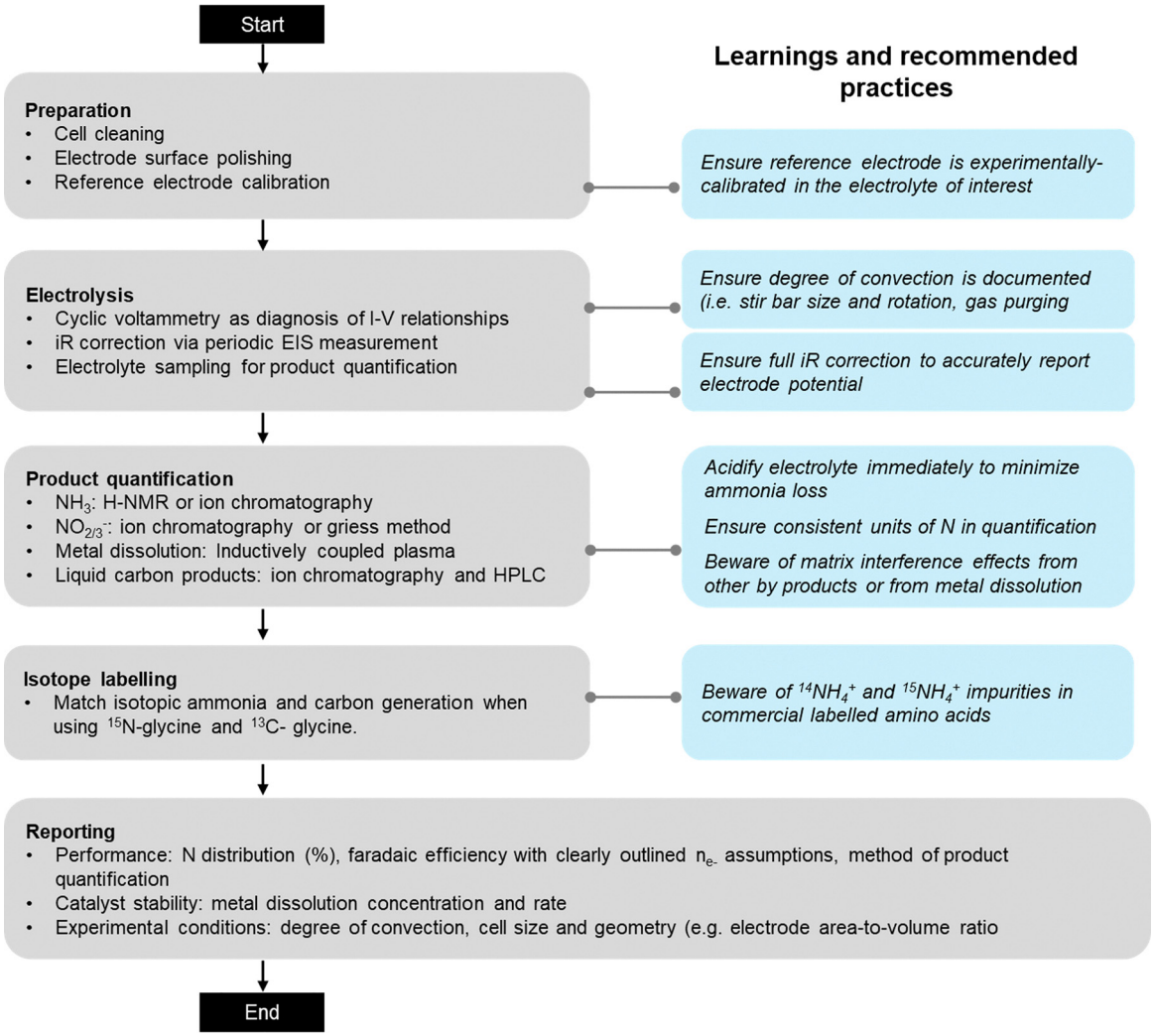

Fig. 7 Proposed experimental protocol for the reliable electrochemical oxidation of glycine and other amino acids. Key learnings and recommended best practices at each stage, including cell and electrode preparation, electrochemical measurements, product detection, and isotope labeling, are summarized in blue on the right for consideration by researchers in the field.

preparation protocols, including immediate electrolyte acidification and appropriate storage. Furthermore, while 15N isotope labeling can provide valuable mechanistic insights, careful interpretation is required due to the presence of 14N-nitrogen impurities observed in this work (Fig. S24). Finally, we recommend comprehensive reporting of scientifically relevant metrics, such as product distributions, Faradaic efficiencies toward nitrogen- and carbon-containing products, and electrode dissolution, together with the corresponding experimental conditions. Particular attention is given to the reporting of pulsing experiments, as the methodology used to account for Faradaic charge such as how capacitive currents are excluded and how anodic and cathodic charges are treated in efficiency calculations can significantly influence quantitative comparisons (Fig. 5) and should therefore be explicitly reported. Such standardized reporting is essential to enable meaningful cross-laboratory comparisons and will be critical for advancing our understanding of electrochemical ammonia recovery from amino acids and organic waste.

Finally, we discuss potential strategies to improve ammonia efficiency and electrode stability based on the trends identified in this work. First, we show that potential pulsing is effective in enhancing ammonia efficiency (Fig. 5). Future efforts can focus on optimizing pulse parameters (potential, duration, and frequency), which have been shown in other systems (*e.g.*, CO_2 reduction[30,31] and urea oxidation[12,27]) to improve selectivity and activity. Second, the observed coupling between ammonia production and Ni dissolution (Fig. 1 and 6) also highlights a fundamental bottleneck. One potential strategy is to decouple amino acid activation (*i.e.*, C–N cleavage) from ammonia stabilization. This may be achieved by leveraging molecular oxidants (*e.g.*, OH^-, H_2O_2)[52,53] to enable amino acid activation at lower potentials, as well as through electrolyte engineering with ionic additives that enhance solution-phase ammonia stability while maintaining environmental compatibility. More urgently, a systematic assessment of Ni stability in real wastewater systems is needed, coupled with chemically resolved characterization of organic nitrogen beyond bulk metrics (*e.g.*, total nitrogen). Notably, prior studies using complex sludge matrices have not reported significant Ni dissolution,[12] suggesting additional matrix effects and/or a surface passivation mechanism that warrants further investigation and may present opportunities for catalyst engineering.

Conclusions

We have conducted a coordinated, cross-institutional study to elucidate the experimentally reproducible features of electrochemical glycine conversion to ammonia. By implementing an identical protocol using polished Ni foil in 0.1 M KOH containing 0.1 M glycine, we demonstrate that ammonia formation occurs under oxidative potentials (>1.60 V_{RHE}), rather than under reducing conditions. Nevertheless, Ni exhibited the lowest overpotential for ammonia production compared to other electrodes, where ammonia was detectably produced only at >2.1 V_{RHE} and >2.6 V_{RHE} for Au and Pt, respectively. At 2.00 V_{RHE} on Ni, ammonia constitutes the dominant solution-phase nitrogen product ($\sim$70% of the nitrogen product distribution), with a faradaic efficiency of 23.0 $\pm$ 2.5%. However, this selectivity is accompanied by substantial Ni dissolution. Comprehensive carbon product analysis of the electrolyte using HPLC, ion chromatography, and ^{13}C NMR reveals the formation of multiple liquid-phase oxidation products, including glycolate, glyoxylate, formaldehyde, cyanide, and formate. Together, these products indicate the presence of parallel reaction pathways involving initial C–N cleavage (pathway 1) and C–C scission (pathway 2) during glycine activation. Complementary thermodynamic analysis further suggests that C–N cleavage may represent the rate-limiting step in both pathways, motivating targeted mechanistic investigations in future studies. Furthermore, extending the study to alanine, lysine, and aspartic acid reveals that ammonia-dominated production correlates with Ni^{2+} dissolution, highlighting Ni complexation as a possible origin of ammonia-dominated production. Importantly, nitrogen selectivity, Ni corrosion rates, and carbon product distributions were found to be highly sensitive to experimental parameters such as stirring rate, electrode area, cell architecture and potential pulsing. Specifically, pulsing to a negative potential was found to robustly increase the ammonia Faradaic efficiency (FE), with mechanistic implications of amine hydrogenation during C–N cleavage as the possible rate-limiting step, but the degree of FE enhancement is highly sensitive to how the positive and negative charges are accounted for. These observations highlight the critical role of the local reaction environment and underscore the need for exhaustive experimental reporting and community-facing best-practice protocols. Although this work focuses on simplified glycine and single-component amino acid systems, it serves as an important foundation for future studies to investigate electrode stability and ammonia production from more complex nitrogen sources (*e.g.*, proteins) and in the presence of other sludge constituents. Increasing system complexity will be essential to advance scalable ammonia recovery from organic waste.

Author contributions

A. J. M., M. C. H., Y. S.-H. and G. B. conceived the idea. H. I., J. A. and D. A. C. H. conducted benchmarking, product quantification and assessment of experimental factors, under the leadership of H. I. Carbon product quantification methodology was developed with the help of D. D. V. Under the supervision of H. I., the pulsing experiments were conducted by A. G. A. The initial draft was prepared by H. I., J. A. and D. A. C. H. All authors were involved in editing and approving the final version of the manuscript.

Conflicts of interest

We declare no conflicts of interest.

Data availability

The data supporting the findings of this study are available in the supplementary information (SI) and from the corresponding

authors upon reasonable request. The supplementary information contains Fig. S1–S44 and Tables S1–S6, including the extended experimental section, calibration curves, electrochemical data, representative spectra for liquid and gas product detection, tabulated experimental values and thermodynamic calculations supporting the results discussed in the manuscript. See DOI: https://doi.org/10.1039/d6ey00044d.

Acknowledgements

This work is based upon financial support by the National Science Foundation, EEC Division of Engineering Education and Centers, NSF Engineering Research Center for Advancing Sustainable and Distributed Fertilizer production (CASFER), NSF 20-553 Gen-4 Engineering Research Centers award # 2133576. H. I. gratefully acknowledges the financial support from the Martin Family Fellowship. D. A. C. H. was partially supported by RBI Graduate Research Fellowship from the Renewable Biproducts Institute at Georgia Institute of Technology. The authors thank Dr. Luisa Barrera and Dr. Nianhan (Kaylee) Tian for their work at the start of the project. Any opinions, findings, and conclusions or recommendations expressed in this material are those of the author(s) and do not necessarily reflect the views of the National Science Foundation.

References

1 Y. Zhou, Y. Zhu, J. Zhu, C. Li and G. Chen, A Comprehensive Review on Wastewater Nitrogen Removal and Its Recovery Processes, *Int. J. Environ. Res. Public Health*, 2023, **20**, 3429.
2 S. Rahimi, O. Modin and I. Mijakovic, Technologies for biological removal and recovery of nitrogen from wastewater, *Biotechnol. Adv.*, 2020, **43**, 107570.
3 P. L. McCarty, What is the Best Biological Process for Nitrogen Removal: When and Why?, *Environ. Sci. Technol.*, 2018, **52**, 3835–3841.
4 X. Hu, *et al.*, Effects of different external carbon sources and electron acceptors on interactions between denitrification and phosphorus removal in biological nutrient removal processes, *J. Zhejiang Univ., Sci., B*, 2018, **19**, 305–316.
5 D. Rosso, L. E. Larson and M. K. Stenstrom, Aeration of large-scale municipal wastewater treatment plants: state of the art, *Water Sci. Technol.*, 2008, **57**, 973–978.
6 G. G. Botte, *et al.*, Innovative Approach to Sustainable Fertilizer Production: Leveraging Electrically Assisted Conversion of Sewage Sludge for Nutrient Recovery, *ACS Omega*, 2024, **9**, 49692–49706.
7 D. A. Chipoco Haro, *et al.*, Electrocatalysts for Inorganic and Organic Waste Nitrogen Conversion, *ACS Catal.*, 2024, **14**, 9752–9775.
8 K. Śpiewak, Gasification of Sewage Sludge—A Review, *Energies*, 2024, **17**(17), 4476.
9 T. N. Trinh, P. A. Jensen, K. Dam-Johansen, N. O. Knudsen and H. R. Sørensen, Influence of the Pyrolysis Temperature on Sewage Sludge Product Distribution, Bio-Oil, and Char Properties, *Energy Fuels*, 2013, **27**, 1419–1427.
10 M. B. Yaala, *et al.*, Plasma-assisted catalytic formation of ammonia in N2–H2 plasma on a tungsten surface, *Phys. Chem. Chem. Phys.*, 2019, **21**, 16623–16633.
11 J. Heberlein and A. B. Murphy, Thermal plasma waste treatment, *J. Phys. D: Appl. Phys.*, 2008, **41**, 053001.
12 M. Jafari and G. G. Botte, Electrochemical valorization of waste activated sludge for short-chain fatty acids production, *Front. Chem.*, 2022, **10**, 974223.
13 R. P. Singh and M. Agrawal, Potential benefits and risks of land application of sewage sludge, *Waste Manage.*, 2008, **28**, 347–358.
14 M. Kacprzak, *et al.*, Sewage sludge disposal strategies for sustainable development, *Environ. Res.*, 2017, **156**, 39–46.
15 S. Hait and V. Tare, Vermistabilization of primary sewage sludge, *Bioresour. Technol.*, 2011, **102**, 2812–2820.
16 M. C. Collivignarelli, *et al.*, What Advanced Treatments Can Be Used to Minimize the Production of Sewage Sludge in WWTPs?, *Appl. Sci.*, 2019, **9**(13), 2650.
17 N. Gao, K. Kamran, C. Quan and P. T. Williams, Thermochemical conversion of sewage sludge: A critical review, *Prog. Energy Combust. Sci.*, 2020, **79**, 100843.
18 W. Hui, J. Zhou and R. Jin, Proteins recovery from waste activated sludge by thermal alkaline treatment, *J. Environ. Chem. Eng.*, 2022, **10**, 107311.
19 S. A. Hoang, *et al.*, Treatment processes to eliminate potential environmental hazards and restore agronomic value of sewage sludge: A review, *Environ. Pollut.*, 2022, **293**, 118564.
20 L. Vriens, R. Nihoul and H. Verachtert, Activated sludges as animal feed: A review, *Biol. Wastes*, 1989, **27**, 161–207.
21 D. G. Marangoni, R. S. Smith and S. G. Roscoe, Surface electrochemistry of the oxidation of glycine at Pt, *Can. J. Chem.*, 1989, **67**, 921–926.
22 P. Sáez-Plaza, T. Michałowski, M. J. Navas, A. G. Asuero and S. Wybraniec, An Overview of the Kjeldahl Method of Nitrogen Determination. Part I. Early History, Chemistry of the Procedure, and Titrimetric Finish, *Crit. Rev. Anal. Chem.*, 2013, **43**, 178–223.
23 J. F. E. Gootzen, A. H. Wonders, W. Visscher, R. A. van Santen and J. A. R. van Veen, A DEMS and cyclic voltammetry study of NH3 oxidation on platinized platinum, *Electrochim. Acta*, 1998, **43**, 1851–1861.
24 F. Huerta, *et al.*, Electrochemical behaviour of amino acids on Pt(*h*,*k*,*l*): a voltammetric and in situ FTIR study. Part 1. Glycine on Pt(111), *J. Electroanal. Chem.*, 1997, **421**, 179–185.
25 L.-C. Chen, T. Uchida, H.-C. Chang and M. Osawa, Adsorption and oxidation of glycine on Au electrode: An in situ surface-enhanced infrared study, *Electrochem. Commun.*, 2013, **34**, 56–59.
26 B. K. Boggs, R. L. Kinga and G. G. Botte, Urea electrolysis: direct hydrogen production from urine, *Chem. Commun.*, 2009, 4859–4861.
27 V. Vedharathinam and G. G. Botte, Understanding the electro-catalytic oxidation mechanism of urea on nickel

electrodes in alkaline medium, *Electrochim. Acta*, 2012, **81**, 292–300.
28 P. C. M. Laan, *et al.*, Understanding the Oxidative Properties of Nickel Oxyhydroxide in Alcohol Oxidation Reactions, *ACS Catal.*, 2023, **13**, 8467–8476.
29 R. Mohan, *et al.*, Electrochemical Oxidation of Glycine with Bimetallic Nickel−Manganese Oxide Catalysts, *ChemElectroChem*, 2020, **7**, 561–568.
30 W. H. Freer, *et al.*, Ammonia production from pulsed electrolysis of amino acids, *J. Appl. Electrochem.*, 2025, **55**, 2561–2571.
31 K. W. Kimura, *et al.*, Controlled Selectivity of CO2 Reduction on Copper by Pulsing the Electrochemical Potential, *ChemSusChem*, 2018, **11**, 1781–1786.
32 Y. Huang, *et al.*, Pulsed electroreduction of low-concentration nitrate to ammonia, *Nat. Commun.*, 2023, **14**, 7368.
33 W. Zheng, *iR* Compensation for Electrocatalysis Studies: Considerations and Recommendations, *ACS Energy Lett.*, 2023, **8**, 1952–1958.
34 C. Wei, *et al.*, Recommended Practices and Benchmark Activity for Hydrogen and Oxygen Electrocatalysis in Water Splitting and Fuel Cells, *Adv. Mater.*, 2019, **31**, 1806296.
35 H. Wan, A. Bagger and J. Rossmeisl, Electrochemical Nitric Oxide Reduction on Metal Surfaces, *Angew. Chem., Int. Ed.*, 2021, **60**, 21966–21972.
36 H. Iriawan, *et al.*, Assessing the Activity of Transition Metal Oxides for the Electrochemical N2 Oxidation to Nitrate, *ACS Catal.*, 2025, **15**, 6315–6333.
37 S. W. Tatarchuk, J. J. Medvedev, F. Li, Y. Tobolovskaya and A. Klinkova, Nickel-Catalyzed Urea Electrolysis: From Nitrite and Cyanate as Major Products to Nitrogen Evolution, *Angew. Chem., Int. Ed.*, 2022, **61**, e202209839.
38 H. K. Thakkar, *et al.*, Vertically Oriented FeNiO Nanosheet Array for Urea and Water Electrolysis at Industrial-Scale Current Density, *ACS Sustainable Chem. Eng.*, 2024, **12**, 8340–8352.
39 T. Kiss, I. Sovago and A. Gergely, Critical survey of stability constants of complexes of glycine, *Pure Appl. Chem.*, 1991, **63**, 597–638.
40 P. R. Varadwaj, I. Cukrowski and H. M. Marques, DFT-UX3LYP Studies on the Coordination Chemistry of Ni^{2+}. Part 1: Six Coordinate $[Ni(NH_3)_n(H_2O)_{6-n}]^{2+}$ Complexes, *J. Phys. Chem. A*, 2008, **112**, 10657–10666.
41 L.-F. Huang, M. J. Hutchison, R. J. Santucci, J. R. Scully and J. M. Rondinelli, Improved Electrochemical Phase Diagrams from Theory and Experiment: The Ni–Water System and Its Complex Compounds, *J. Phys. Chem. C*, 2017, **121**, 9782–9789.
42 R. Hudson, *et al.*, CO_2 reduction driven by a pH gradient, *Proc. Natl. Acad. Sci. U. S. A.*, 2020, **117**, 22873–22879.
43 I. G. Shenderovich, G. S. Denisov, I. G. Shenderovich and G. S. Denisov, NMR Properties of the Cyanide Anion, a Quasisymmetric Two-Faced Hydrogen Bonding Acceptor, *Symmetry*, 2021, **13**(7), 1298.
44 K. Das, J. Dumais, S. Basiaga and G. D. Krzyzanowski, Carbon-13 nuclear magnetic resonance analysis of formaldehyde free preservatives, *Acta Histochem.*, 2013, **115**, 481–486.
45 C. Butch, *et al.*, Production of Tartrates by Cyanide-Mediated Dimerization of Glyoxylate: A Potential Abiotic Pathway to the Citric Acid Cycle, *J. Am. Chem. Soc.*, 2013, **135**, 13440–13445.
46 S. C. Cheng, M. Gattrell, T. Guena and B. MacDougall, The electrochemical oxidation of alkaline copper cyanide solutions, *Electrochim. Acta*, 2002, **47**, 3245–3256.
47 H. Xu, A. Li, L. Feng, X. Cheng and S. Ding, Destruction of Cyanide in Aqueous Solution by Electrochemical Oxidation Method, *Int. J. Electrochem. Sci.*, 2012, **7**, 7516–7525.
48 I. Zelitch and A. Gotto, Properties of a new glyoxylate reductase from leaves, *Biochem. J.*, 1962, **84**, 541–546.
49 Y.-F. Li and A. Selloni, Mechanism and Activity of Water Oxidation on Selected Surfaces of Pure and Fe-Doped NiOx, *ACS Catal.*, 2014, **4**, 1148–1153.
50 Y. J. Son, *et al.*, Effects of Electrochemical Conditioning on Nickel-Based Oxygen Evolution Electrocatalysts, *ACS Catal.*, 2022, **12**, 10384–10399.
51 S. Klaus, Y. Cai, M. W. Louie, L. Trotochaud and A. T. Bell, Effects of Fe Electrolyte Impurities on $Ni(OH)_2$/NiOOH Structure and Oxygen Evolution Activity, *J. Phys. Chem. C*, 2015, **119**, 7243–7254.
52 R. Drozdź, J. W. Naskalski and J. Sznajd, Oxidation of amino acids and peptides in reaction with myeloperoxidase, chloride and hydrogen peroxide, *Biochim. Biophys. Acta, Protein Struct. Mol. Enzymol.*, 1988, **957**, 47–52.
53 E. R. Stadtman and B. S. Berlett, Fenton chemistry. Amino acid oxidation, *J. Biol. Chem.*, 1991, **266**, 17201–17211.
54 N. Mahne, *et al.*, Singlet oxygen generation as a major cause for parasitic reactions during cycling of aprotic lithium–oxygen batteries, *Nat. Energy*, 2017, **2**, 17036.
55 G. Chen, *et al.*, A discussion on the possible involvement of singlet oxygen in oxygen electrocatalysis, *J. Phys. Energy*, 2021, **3**, 031004.
56 H. A. Hansen, J. Rossmeisl and J. K. Nørskova, Surface Pourbaix diagrams and oxygen reduction activity of Pt, Ag and Ni(111) surfaces studied by DFT, *Phys. Chem. Chem. Phys.*, 2008, **10**, 3722–3730.
57 L. Trotochaud, S. L. Young, J. K. Ranney and S. W. Boettcher, Nickel–Iron Oxyhydroxide Oxygen-Evolution Electrocatalysts: The Role of Intentional and Incidental Iron Incorporation, *J. Am. Chem. Soc.*, 2014, **136**, 6744–6753.
58 I. Zilbermann, E. Maimon, H. Cohen and D. Meyerstein, Redox Chemistry of Nickel Complexes in Aqueous Solutions, *Chem. Rev.*, 2005, **105**, 2609–2626.
59 B. J. Green, T. M. Tesfai and D. W. Margerum, Nickel(III) oxidation of its glycylglycylhistamine complex, *Dalton Trans.*, 2004, 3508, DOI: 10.1039/b409929j.
60 X. Liu, *et al.*, Interaction Structure and Affinity of Zwitterionic Amino Acids with Important Metal Cations (Cd^{2+}, Cu^{2+}, Fe^{2+}, Hg^{2+}, Mn^{2+}, Ni^{2+} and Zn^{2+}) in Aqueous Solution: A Theoretical Study, *Molecules*, 2022, **27**, 2407.